

## DYNAMICS OF EMERGING FLUX TUBES IN THE SUN

T. MAGARA

Department of Physics, Montana State University, Bozeman, MT 59717-3840; magara@solar.physics.montana.edu

Received 2000 July 31; accepted 2000 November 3

### ABSTRACT

This paper is intended to study the evolution of a magnetic flux tube that rises from the upper convection zone to the solar atmosphere by means of a 2.5-dimensional MHD simulation with the focus on the cross section of the flux tube. A cylindrical flux tube placed horizontally in the convection zone starts rising by magnetic buoyancy. When the top of the tube reaches the photosphere, the cross section of the tube changes from the circular shape to horizontally extended shape, forming a magnetic layer under the contact surface between the tube and the photosphere. As the plasma inside that magnetic layer is squeezed out to both sides of the layer, the contact surface is locally subject to the Rayleigh-Taylor instability because the lighter magnetic layer is overlain by the heavier photospheric layer. The wavelength of the undulating magnetic layer at the contact surface increases as the flattening of the tube proceeds, and after it becomes longer than the critical wavelength for the Rayleigh-Taylor instability, the tube can emerge through the photosphere. The emergence part of the tube starts expanding into the atmosphere if it has a sufficiently strong magnetic pressure compared to the surrounding gas pressure. We find that this expansion process is characterized by a self-similar behavior, that is, both the plasma and the magnetic field have a steady distribution in the expanding area. On the basis of those results, we try to clarify several important features of emerging flux tubes expected from observations. We focus on two solar phenomena, the birth of emerging flux tubes and the formation of filaments, and discuss the physical processes related to these phenomena.

*Subject headings:* MHD — Sun: atmosphere — Sun: filaments — Sun: magnetic fields

### 1. INTRODUCTION

Recently, magnetic flux tubes have been among the most attractive objects that draw the attention of many solar physicists. They are now believed to be connected with a variety of phenomena observed in the Sun, such as tiny bipoles, arch filament systems, sunspots, filaments, X-ray brightenings, coronal mass ejections, the sigmoid structure of coronal arcades, and so on (Tanaka 1991; Thomas & Weiss 1992; Ishii, Kurokawa, & Takeuchi 1998; Yoshimura & Kurokawa 1999; Kankelborg & Longcope 1999; Canfield, Hudson, & McKenzie 1999). It is therefore important to clarify the dynamics of flux tubes in various situations in order to understand the physical mechanisms of these kinds of phenomena. The behavior of flux tubes in the convection zone has been studied extensively by means of the thin flux tube model (Spruit 1981). Choudhuri & Gilman (1987) investigated the latitude where flux tubes emerge through the convection zone, and they concluded that the magnetic field of flux tubes at the bottom of the convection zone is more than  $10^4$  G, the equipartition value to the convective motion at that layer. Howard (1991) determined the dependence of the tilt angle of emerging bipolar systems on the latitude, and the calculation by D'Silva & Choudhuri (1993) successfully reproduced this dependence assuming that the initial strength of the magnetic field is  $10^5$  G at the bottom of the convection zone. Caligari, Moreno-Insertis, & Schüssler (1995) performed three-dimensional simulations of a flux tube rising from the bottom to the top of the convection zone and illustrated the asymmetric proper motion of sunspots. Fisher, Fan, & Howard (1995) investigated the relation between tilt angle and net flux of bipoles.

While the thin flux tube model provides little information on the deformation process of the cross section of rising flux tubes, several two- or 2.5-dimensional MHD simulations have clarified this process for a cylindrical flux tube placed horizontally in the convection zone. Schüssler (1979) studied a flux tube without any twisting magnetic field (untwisted flux tube) and found that the initial circular cross section was changed into an umbrella shape with an arc-shaped edge. Longcope, Fisher, & Arendt (1996) also discovered that a rising flux tube was subject to both the deformation and decomposition effects so that it finally stopped rising. Emonet & Moreno-Insertis (1998) studied the effect of field line twist on the tube dynamics, suggesting that the strong twist can suppress the deformation of the cross section, making the tube rise continuously.

Detailed studies have also been carried out on the behavior of the magnetic field rising from the upper convection zone to the solar atmosphere (Shibata et al. 1989; Kaisig et al. 1990; Nozawa et al. 1992; Yokoyama & Shibata 1996). This series of works assumes a horizontal flux sheet initially placed under the photosphere, which later emerges to the atmosphere by magnetic buoyancy instability (Parker instability). Shibata et al. (1989) discovered a self-similar expansion process of the magnetic field in the nonlinear stage of the Parker instability by performing two-dimensional MHD simulations. This process was later considered in more detail by an analytical method in Shibata, Tajima, & Matsumoto (1990). Nozawa et al. (1992) discussed the effect of convective collapse at the footpoints of an expanding loop, while Yokoyama & Shibata (1996) studied the magnetic reconnection between the expanding magnetic field and the overlying field.

The works introduced above have explored the expansion process of flux sheets in the atmosphere, while here we focus our attention on discrete flux tubes and investigate their emergence and expansion processes in the atmosphere. The study lying in this line of works is found in Krall et al. (1998), in which they studied the rise process of a flux tube in the chromosphere and

the corona. Compared to their study, the scope of the present study includes the emergence process of a flux tube from the upper convection zone to the atmosphere. We start with a cylindrical flux tube placed horizontally in the convection zone, which later rises by magnetic buoyancy. We then see how the cross section of the tube evolves as the tube rises from the upper convection zone to the atmosphere by means of 2.5-dimensional MHD simulation. Compared to the previous two-dimensional flux-sheet studies, the present work shows some similar effects because the same physical mechanism (magnetic buoyancy) makes an important contribution to the evolution. On the other hand, the twisted structure of the magnetic field neglected in the flux-sheet studies brings us some new important aspects of magnetic field emergence on the Sun, which we discuss in detail in this paper. These new aspects, combined with what the flux-sheet studies have clarified, give us important insight into the three-dimensional evolution of emerging flux tubes (Matsumoto et al. 1998).

We give an overall description of our model in the next section. The results are shown in § 3, which are discussed in detail in § 4 with special attention paid to the connection with observational results. Finally, we summarize this work in § 5.

2. MODEL DESCRIPTION

2.1. Basic Equations

In order to study the dynamics of flux tubes in a stratified atmosphere, we use the standard set of MHD equations that includes the gravitational force while the effects of resistivity and viscosity are neglected. These are explicitly written as follows:

$$\frac{\partial \rho}{\partial t} + \nabla \cdot (\rho \mathbf{v}) = 0, \tag{1}$$

$$\rho \left[ \frac{\partial \mathbf{v}}{\partial t} + (\mathbf{v} \cdot \nabla) \mathbf{v} \right] = -\nabla P + \frac{1}{4\pi} (\nabla \times \mathbf{B}) \times \mathbf{B} + \rho \mathbf{g}, \tag{2}$$

$$\frac{\rho^\gamma}{\gamma - 1} \left[ \frac{\partial}{\partial t} \left( \frac{P}{\rho^\gamma} \right) + (\mathbf{v} \cdot \nabla) \left( \frac{P}{\rho^\gamma} \right) \right] = 0, \tag{3}$$

$$\frac{\partial \mathbf{B}}{\partial t} = \nabla \times (\mathbf{v} \times \mathbf{B}), \tag{4}$$

and

$$P = \frac{\rho \mathfrak{R} T}{\mu}, \tag{5}$$

where  $\rho$ ,  $\mathbf{v}$ ,  $\mathbf{B}$ ,  $P$ ,  $\mathbf{g}$ ,  $\gamma$ ,  $\mu$ ,  $\mathfrak{R}$ , and  $T$  denote the gas density, flow velocity, magnetic field, gas pressure, gravitational acceleration, adiabatic index, mean molecular weight, gas constant, and temperature, respectively. In the actual calculations, we use the nondimensional form of those equations, which is derived from introducing a naturalized unit for every physical quantity. The collection of these units is exhibited in Table 1.

2.2. Initial Conditions

We use the Cartesian coordinate system to model the local area extending from the upper convection zone to the corona. The  $(x, y)$ -plane is located at the photospheric level, and the  $z$ -coordinate is vertically increasing upward. This study is based on the 2.5-dimensional numerical simulation, which means that all the physical quantities are translationally invariant along the  $y$ -axis while the  $y$ -component of vector quantities is taken into our consideration. The initial distributions of plasma

TABLE 1  
UNITS OF PHYSICAL QUANTITIES

Physical Quantity	Unit	Real Value
Length (cm) .....	$2\Lambda_p$	$3.0 \times 10^7$
Velocity (km s <sup>-1</sup> ) .....	$C_{Sp}$	8.6
Time (s) .....	$2\Lambda_p/C_{Sp}$	35
Density (g cm <sup>-3</sup> ) .....	$\rho_p$	$2.7 \times 10^{-7}$
Pressure (dynes cm <sup>-2</sup> ) .....	$\gamma P_p$	$2.0 \times 10^5$
Temperature (K) .....	$T_p$	5100
Gravitational acceleration (m s <sup>-2</sup> ) .....	$(\gamma/2)g_p$	290
Magnetic field (G) .....	$(\rho C_{Sp})^{1/2}$	450

NOTE.— $\Lambda \equiv P\rho^{-1}g^{-1}$  and  $C_s \equiv (\gamma\mathfrak{R}T\mu^{-1})^{1/2}$  are the pressure scale height and adiabatic sound velocity, respectively. Subscript  $p$  indicates the photospheric value. Here we assume  $\rho_p = 2.7 \times 10^{-7}$  g cm<sup>-3</sup>,  $P_p = 1.2 \times 10^5$  dynes cm<sup>-2</sup>,  $\Lambda_p = 150$  km,  $C_{Sp} = 8.6$  km s<sup>-1</sup>,  $g_p = 340$  m s<sup>-2</sup>, and  $T_p = 5100$  K.

quantities are expressed as follows:

$$\mathbf{g}(z) = g(z)\hat{\mathbf{z}} = -g_p\hat{\mathbf{z}}, \quad (6)$$

$$T(z) = \begin{cases} T_p - S_a \left| \frac{dT}{dz} \right|_{\text{ad}} f(z) & (z_{\text{conv}} \leq z < z_p) \\ T_p + (T_c - T_p) \left\{ \frac{1}{2} \left[ \tanh \left( \frac{z - z_t}{w_t} \right) + 1 \right] \right\} & (z_p \leq z < z_t) \\ \left( T_p + (T_c - T_p) \left\{ \frac{1}{2} \left[ \tanh \left( \frac{z - z_t}{w_t} \right) + 1 \right] \right\} \right) \left( \frac{z - z_t}{z_{\text{cor}} - z_t} + 1 \right) & (z_t \leq z < z_{\text{cor}}) \\ \left( T_p + (T_c - T_p) \left\{ \frac{1}{2} \left[ \tanh \left( \frac{z - z_t}{w_t} \right) + 1 \right] \right\} \right) 2 & (z_{\text{cor}} \leq z) \end{cases}, \quad (7)$$

$$P(z) = P_p \exp \left[ - \int_{z_p}^z \frac{\gamma g(z')}{T(z')} dz' \right], \quad (8)$$

and

$$\rho(z) = \frac{\gamma P(z)}{T(z)}, \quad (9)$$

where  $\gamma = 5/3$ ,  $g_p = 2/\gamma = 1.2$ ,  $|dT/dz|_{\text{ad}} = 2(\gamma - 1)/\gamma = 0.4$ ,  $T_p = 1$ ,  $T_c = 100$ ,  $P_p = 1/\gamma = 0.6$ ,  $z_{\text{conv}} = -10$ ,  $z_p = 0$ ,  $z_t = 7.5$ ,  $z_{\text{cor}} = 20$ , and  $w_t = 0.5$  in nondimensional form. (Hereafter all the physical quantities are expressed in nondimensional form.)  $S_a \equiv |dT/dz|/|dT/dz|_{\text{ad}}$  represents the superadiabaticity of the convection layer, chosen to be 1.025 in this simulation. The function  $f(z)$  provides the smooth connection of the temperature gradient between  $|dT/dz| = 0$  in the photosphere and  $|dT/dz| = S_a |dT/dz|_{\text{ad}} = 0.41$  in the convection layer, whose explicit form is

$$f(z) = \frac{1}{4} \ln \left\{ \frac{\cosh(2z_p)}{\cosh[2(z - z_p)]} \right\} + \frac{z}{2}. \quad (10)$$

In order to provide the initial distribution of the magnetic field, we use the so-called Gold-Hoyle flux tube model expressed as

$$B_x = -B_0 \frac{b(z - z_0)}{1 + b^2[(x - x_0)^2 + (z - z_0)^2]}, \quad (11)$$

$$B_y = B_0 \frac{1}{1 + b^2[(x - x_0)^2 + (z - z_0)^2]}, \quad (12)$$

and

$$B_z = B_0 \frac{b(x - x_0)}{1 + b^2[(x - x_0)^2 + (z - z_0)^2]}, \quad (13)$$

where  $(x_0, z_0)$  is the tube center,  $b$  is the twist parameter, and  $B_0$  is the strength of the magnetic field at the tube center. Then we divide the distribution of the magnetic field into two areas, that is,  $r \leq r_t$  is the area of a flux tube and  $r > r_t$  is the area of an external field, where  $r \equiv [(x - x_0)^2 + (z - z_0)^2]^{1/2}$  and  $r_t$  is the tube radius. Both areas are different in terms of the parameters  $B_0$  and  $b$ . In this simulation, we choose the position of the tube center and the parameters of the external field as  $x_0 = 0$ ,  $z_0 = z_p - 6 = -6$ ,  $B_0 = 1.23$ , and  $b = 50$ . On the other hand, we change those parameters characterizing the tube and provide several models of the flux tube, which are summarized in Table 2. In general we have three free parameters

TABLE 2  
SUMMARY OF MODELS

Model	$r_t^a$	$b^b$	$B_0^c$	$B_b^d$	$\beta_0^e$
T .....	2.0 (600 km)	4.09	17.4 (7760 G)	2.11 (941 G)	8.32
WB .....	2.0 (600 km)	2.00	8.68 (3880 G)	2.11 (941 G)	33.3
Lr .....	3.0 (900 km)	1.33	8.68 (3880 G)	2.11 (941 G)	33.3
Sr .....	1.0 (300 km)	4.00	8.68 (3880 G)	2.11 (941 G)	33.3

NOTE.—Model T is a typical case. Models WB, Lr, and Sr represent the cases of weaker magnetic field, larger radius, and smaller radius compared to model T. The number in parentheses represents a real value.

<sup>a</sup> Radius of the tube.

<sup>b</sup> Twist parameter.

<sup>c</sup> Strength of the magnetic field at the tube center.

<sup>d</sup> Strength of the magnetic field at the tube boundary.

<sup>e</sup> Plasma beta at the tube center.

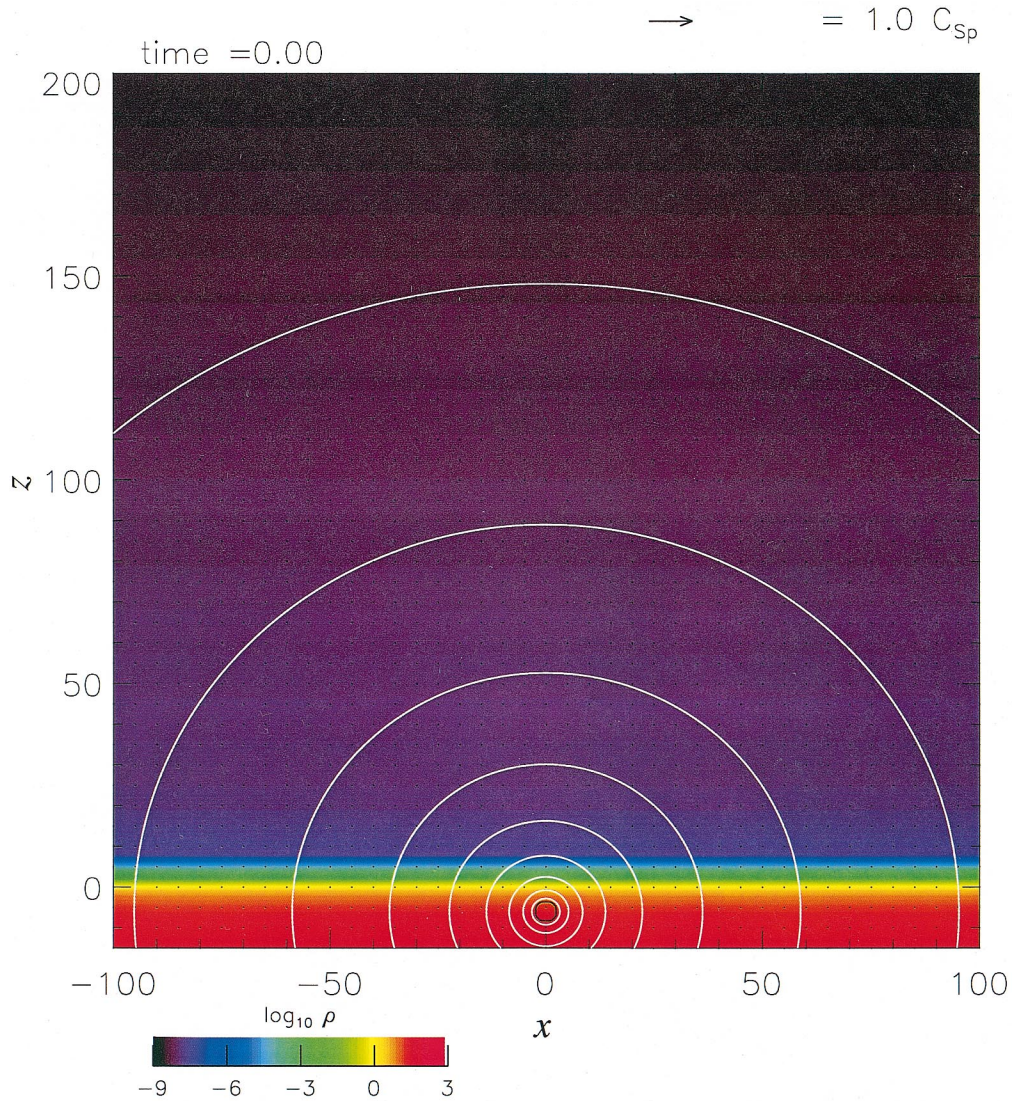
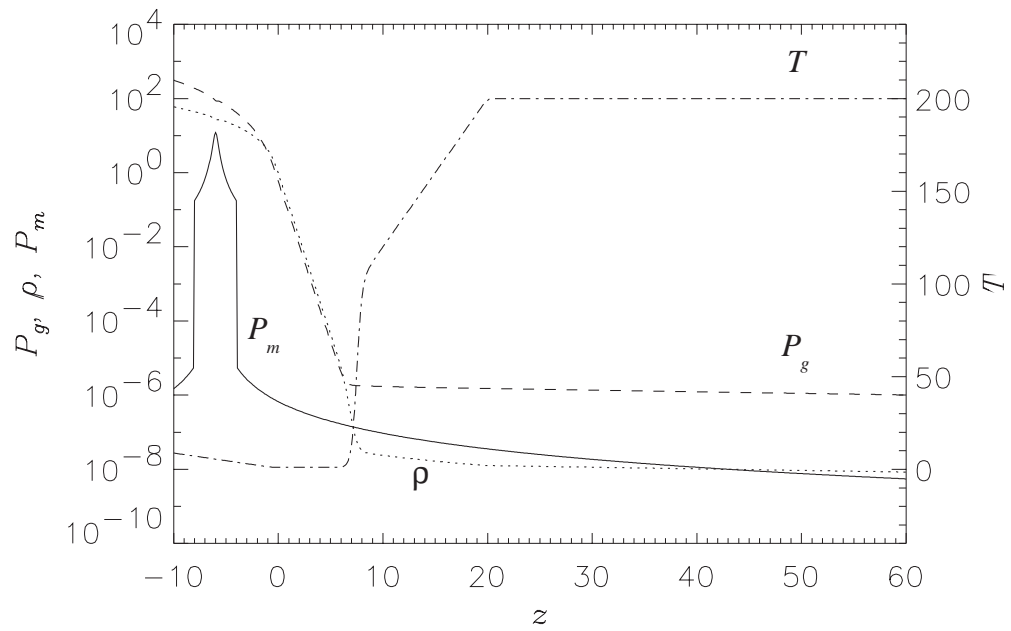


FIG. 1.—(a) Initial distributions of magnetic pressure (solid line), gas pressure (dashed line), gas density (dotted line), and temperature (dot-dashed line) along the  $z$ -axis for model T. (b) Two-dimensional view graph of the initial configuration for model T. A black circle shows the boundary of the flux tube, and white contour lines represent external magnetic field lines. A color map shows gas density.

characterizing the flux tube,  $r_t$ ,  $B_0$ , and  $b$ , although here we assume one constraint, that the magnetic energy density is comparable to the convective energy density at the tube boundary. This means that while taking a long journey through the convection zone, a flux tube obtains such a strong magnetic field as to counteract convective motion. When we write the convective energy density as  $\mathcal{E}_c$ , then this constraint is expressed as

$$\frac{B_0^2}{8\pi} \frac{1}{b^2 r_t^2} \sim \mathcal{E}_c. \quad (14)$$

In this study, we adopt  $\mathcal{E}_c \equiv 1/2 \rho_{\text{conv}} v_{\text{conv}}^2 = 0.23$ , where  $\rho_{\text{conv}} = 15(4.0 \times 10^{-6} \text{ g cm}^{-3})$  and  $v_{\text{conv}} = 0.17(1.5 \text{ km s}^{-1})$  at  $z = -3.5$  (1050 km below the photosphere). These values are based on the typical property of the convective motion in the upper convection zone (Stix 1991). Consequently, the ratio of the magnetic energy density to the convective energy density at the tube boundary is 1.3 for all the models shown in Table 2.

Since the Gold-Hoyle magnetic field is a force-free field, the magnetic force and the other forces exerted on a plasma are completely decoupled, maintaining the force balance separately everywhere except the tube area, in which the gas pressure, temperature, and density are defined as

$$P_{\text{tube}}(x, z) = P(z) - \frac{B_0^2}{8\pi} \frac{1}{1 + b^2 r^2}, \quad (15)$$

$$T_{\text{tube}}(z) = T(z), \quad (16)$$

and

$$\rho_{\text{tube}}(x, z) = \gamma \frac{P_{\text{tube}}(x, z)}{T_{\text{tube}}(z)}, \quad (17)$$

where  $T(z)$  and  $P(z)$  are given by equations (7) and (8). Here we assume that the temperature does not change across the tube boundary so that the density inside the tube is smaller than the outside, which leads to the rising of the tube.

We use model T to show the initial distributions of the gas pressure, density, temperature, and magnetic pressure along the  $z$ -axis in Figure 1a. We also show a two-dimensional view graph of the initial configuration for model T projected onto the  $(x, z)$ -plane in Figure 1b, where the tube boundary, external magnetic field lines, gas density, and flow velocity field are shown by a black circle, white contour lines, a color map, and arrows, respectively. The span of horizontal axis in Figure 1a is part of the full vertical range of the calculation domain, while Figure 1b shows the total simulation area (see § 2.3).

### 2.3. Calculation Method

The numerical code of this simulation is based on the modified Lax-Wendroff method including the artificial viscosity, details of which can be seen in Magara (1998). This code, and others like it, have been used extensively in the past (Shibata et al. 1989; Kaisig et al. 1990; Nozawa et al. 1992; Yokoyama & Shibata 1996; Moreno-Insertis & Emonet 1996; Magara & Shibata 1999).

The total calculation domain is  $(-100, -15) \leq (x, z) \leq (100, 200)$ , though we actually calculate a half of this domain  $(0, -15) \leq (x, z) \leq (100, 200)$ , assuming symmetry with respect to the  $z$ -axis (see Fig. 1b). The top, bottom, and side boundaries are fixed boundaries where all the physical quantities keep their initial values, whereas the symmetric axis is an antisymmetric boundary. We also set a wave-damping region near the top ( $190 \leq z \leq 200$ ), bottom ( $-15 \leq z \leq -10$ ), and side ( $90 \leq x \leq 100$ ) boundaries, which reduces the effect of reflected waves generated at those fixed boundaries. The top and bottom wave-damping regions are made to be an isothermal and nonstratified layer in this simulation.

The mesh size  $(\Delta x, \Delta z)$  is nonuniform along both the  $x$ - and  $z$ -axes. The area of  $(0, -15) \leq (x, z) \leq (10, 10)$  is a fine-mesh area where  $(\Delta x, \Delta z) = (0.1, 0.1)$ , while both mesh sizes gradually increase toward 1.0 with  $x$  and  $z$ . Consequently, the total mesh number is  $N_x \times N_z = 223 \times 473$ , where  $N_x$  and  $N_z$  represent the number of meshes along the  $x$ - and  $z$ -axes, respectively.

## 3. RESULTS

### 3.1. Overall Evolution

First, we use model T to show the overall evolution of the cross section of the tube from the upper convection zone to the corona. Figures 2a–2f display a close-up of the area around the tube, where the black contour line, white contour lines, arrows, and the color map represent the boundary of the tube, magnetic field lines, flow velocity field, and gas density, respectively. Figure 2a presents the initial state, and Figure 2b shows how the tube rises through the convection zone. This figure also shows the large velocity in the region above the photosphere, which is caused by the amplification of the propagating convective motions induced by a rising tube. In Figure 2c the top of the tube reaches the photosphere and then it starts emerging into the atmosphere (Fig. 2d). The following dynamical behavior in the expansion phase can be found in Figures 2e and 2f.

Next let us follow the tracers of several chosen points located on the tube in this evolution. These points are located at the top, center, and bottom of the tube, each of which is represented by A, B, and C, respectively (see Fig. 3a). Figure 3a shows the position of those points along the  $z$ -axis as a function of time, while Figure 3b is the time-derivative version of Figure 3a, that is, it shows how the velocities of A, B, and C change with time in the Lagrangian frame. When we focus on the velocity change of A in Figure 3b, we can see that there are several distinct phases in the evolution: the initial phase when the rise velocity gradually increases (Phase I,  $0 \leq t \leq 35$ ), the second phase when this acceleration process becomes suppressed (Phase II,  $35 \leq t \leq 50$ ), the third phase when the rise velocity starts increasing again (Phase III, around  $t = 50$ ), and the final phase when

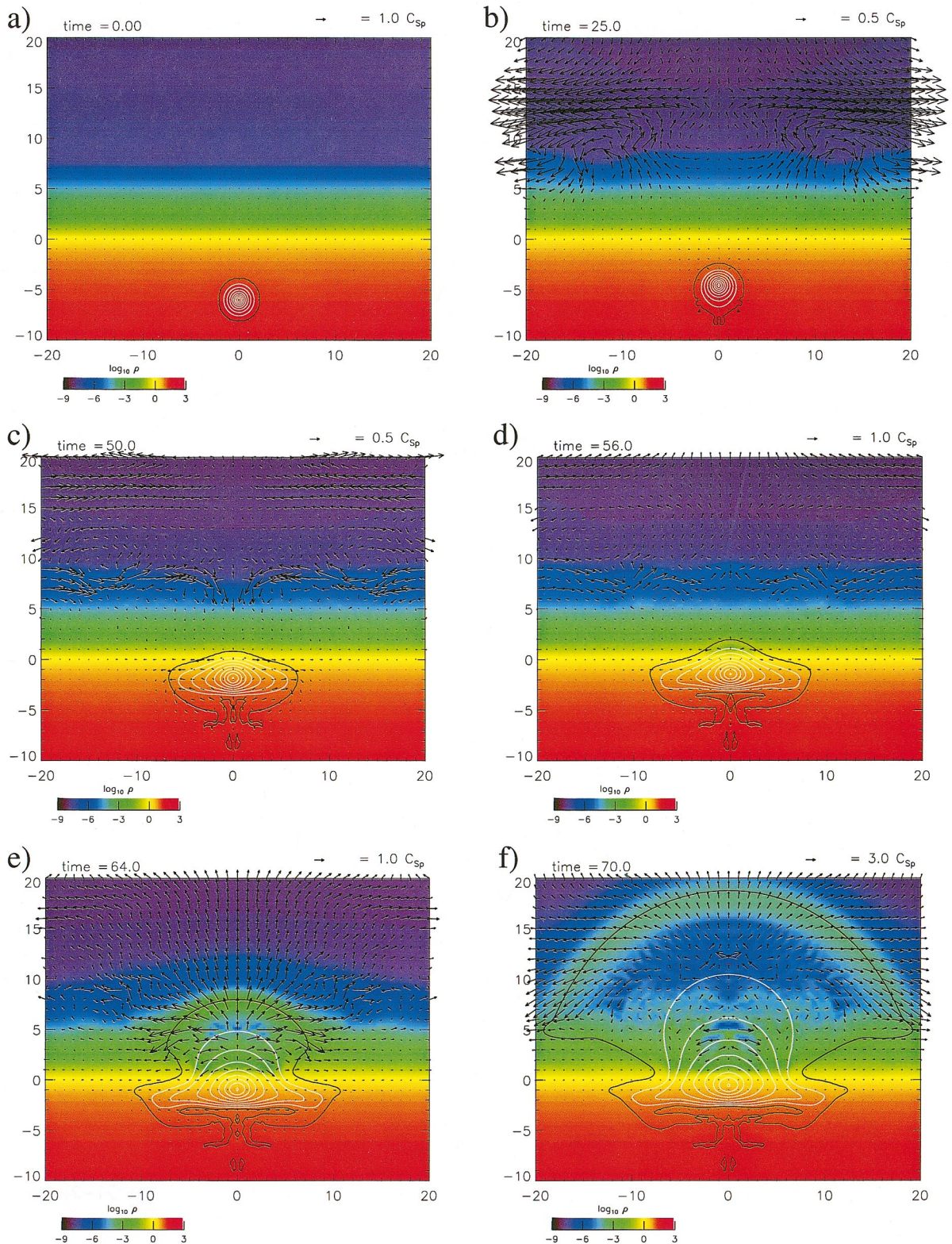


FIG. 2.—Two-dimensional view graphs showing the evolution of flux tube for model T. (a)  $t = 0$ ; (b)  $t = 25$ ; (c)  $t = 50$ ; (d)  $t = 56$ ; (e)  $t = 64$ ; (f)  $t = 70$ . A black contour line, white contour lines, arrows, and a color map show the boundary of the flux tube, magnetic field lines, flow velocity field, and gas density, respectively. The unit of velocity is given by the adiabatic sound velocity in the photosphere for  $t = 0, 56$ , and  $64$ , a half sound velocity for  $t = 25$  and  $50$ , and 3 times sound velocity for  $t = 70$ .

the rise velocity is extremely enhanced (Phase IV,  $t \geq 55$ ). All of these phases are important ingredients composing the evolution of an emerging flux tube, so that we make a detailed investigation on each phase in the following.

3.1.1. Phase I ( $0 \leq t \leq 35$ )

In this phase, a flux tube rises through the convection zone by magnetic buoyancy. In addition, this layer is convectively

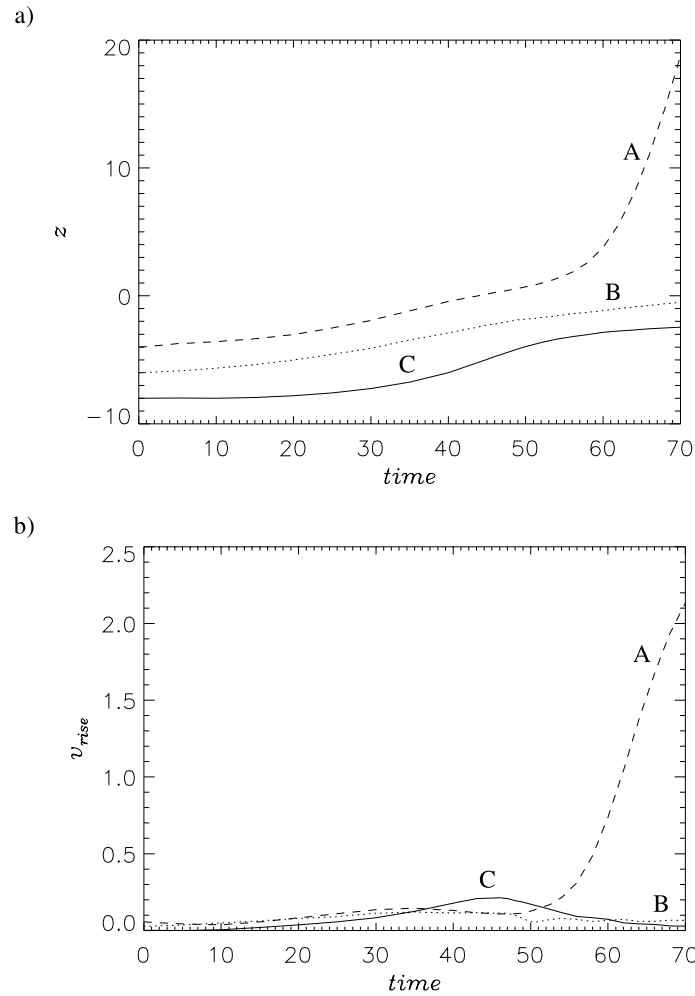


FIG. 3.—(a) Height-time relation of several tracers initially located at the top (A), the center (B), and the bottom (C) of the flux tube for model T. (b) Time variation of the Lagrangian velocities of A, B, and C.

unstable so that continuous convective motion arises, which supports the rising of the tube. Since the tube almost keeps the initial circular cross section during this phase (see Fig. 2b), we can safely study the dynamics by using the model of a rigid cylinder rising in a gravitationally stratified layer. According to this model, the motion of a cylinder is described by the following momentum equation:

$$(M + m_i) \frac{d^2 z}{dt^2} = -(M - m_i)g . \quad (18)$$

Here  $M$  and  $m_i$  are the mass of cylinder and the induced mass per unit length in the axial direction, respectively. We derive  $M = 427$  and  $m_i = 430$  from the initial state of model T, which gives the velocity change with time as follows:

$$v_z \equiv \frac{dz}{dt} = -\frac{M - m_i}{M + m_i} gt = 4.09 \times 10^{-3} t . \quad (19)$$

The velocity development given by equation (19) is represented by a solid line in Figure 4. This is a close-up view of the evolution between  $t = 0$  and  $t = 40$  of Figure 3b, showing how the velocity of the top of the tube changes with time (*dashed line*). From this figure it is found that a rigid cylinder model explains the simulation result quite well except for the nonzero velocity in the very early stage, which is caused by the quick response of the tube to the nonequilibrium environment at the initial state.

### 3.1.2. Phase II ( $35 \leq t \leq 50$ )

The continuous rise motion along the symmetric axis generated in the convection zone cannot persist through the photosphere because the photosphere is a convectively stable layer that inhibits the unidirectional gas motion. This can be seen in Figure 5, which displays the distribution of the vertical component of velocity along the  $z$ -axis at three different times ( $t = 25$ , *solid line*;  $t = 35$ , *dotted line*;  $t = 45$ , *dashed line*). The distribution of magnetic flux at those times is also displayed at the lower part of this figure (the value has been scaled), which represents the position of the flux tube along the symmetric axis at the corresponding times. This figure shows that the unidirectional rise motion in the convection zone is changed into the

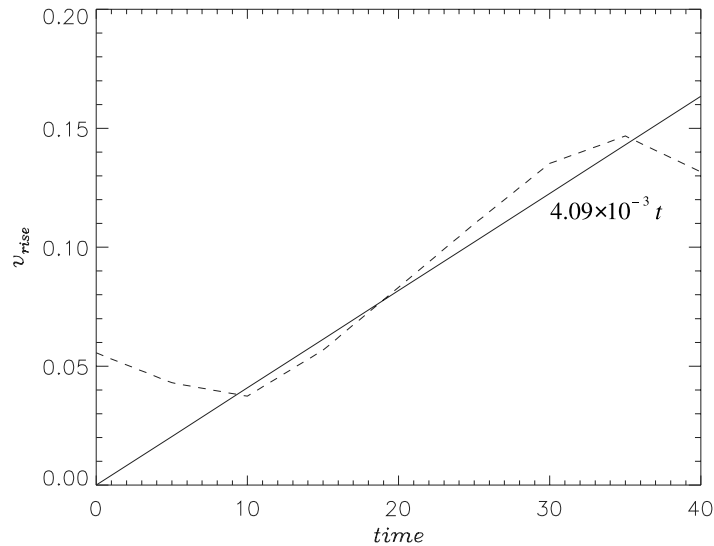


FIG. 4.—Time variation of the Lagrangian velocity of A (*dashed line*). A solid line shows the velocity development based on the rigid cylinder model.

oscillatory motion around the photosphere. The change of the mode of motion causes the tube to decelerate when the tube comes close to the photosphere, which can be seen in Figure 4 (see  $t \geq 30$ ). Another point to be noticed is that the shape of the cross section becomes flattened because the top of the tube slows down while the lower part of the tube is still in the convection zone with high rise velocity (see Fig. 2c). This is quite different from the case in which the tube is wholly inside the convection zone, where the tube has almost the same rise velocity along the symmetric axis (see  $t = 25$  in Fig. 5) and shows no strong deformation (see Fig. 2b).

3.1.3. Phase III ( $t \sim 50$ )

As the tube is flattened, the magnetic field under the contact surface becomes parallel to the surface. A magnetic layer is formed locally under that contact surface, and furthermore the plasma inside this layer is squeezed out to both sides of the layer by the horizontal surface flows (see Fig. 2c). Consequently, the contact surface becomes subject to the so-called Rayleigh-Taylor instability because a gas layer with heavier plasma is located on top of a magnetic layer with lighter plasma. This is schematically shown in Figure 6a. We also show the vertical distributions of the magnetic pressure (*solid line*), gas pressure (*dotted line*), and gas density (*dashed line*) around the contact surface in Figure 6b. This figure indicates that the density reduction occurs in the magnetic layer.

We here investigate the behavior of the magnetic layer in terms of the Rayleigh-Taylor instability. When we take into account the fact that the magnetic field under the contact surface is almost  $x$ -directional, the dispersion relation of this instability in the present configuration is expressed as follows:

$$\omega^2 = -gk_x \frac{\rho_0^+ - \rho_0^-}{\rho_0^+ + \rho_0^-} + k_x^2 \frac{B_{0x}^{-2}}{4\pi(\rho_0^+ + \rho_0^-)}, \tag{20}$$

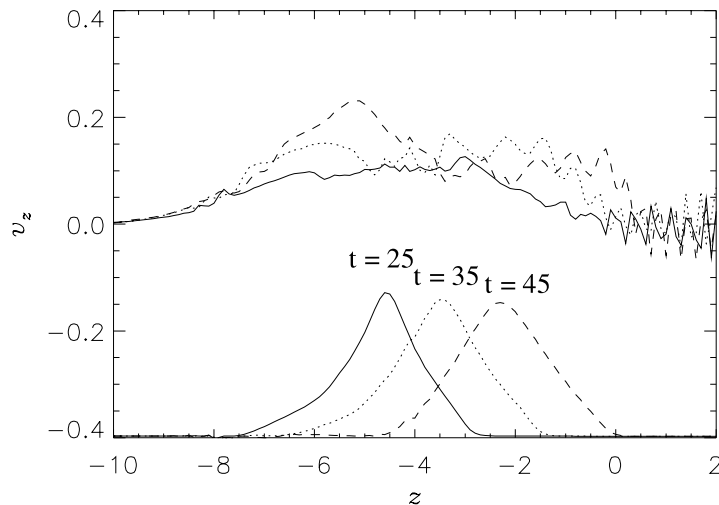


FIG. 5.—Distribution of the vertical component of velocity along the  $z$ -axis for model T. Solid, dotted, and dashed lines represent the distribution at  $t = 25, 35,$  and  $45,$  respectively. At the lower part of the figure is the distribution of magnetic flux along the  $z$ -axis at those times.

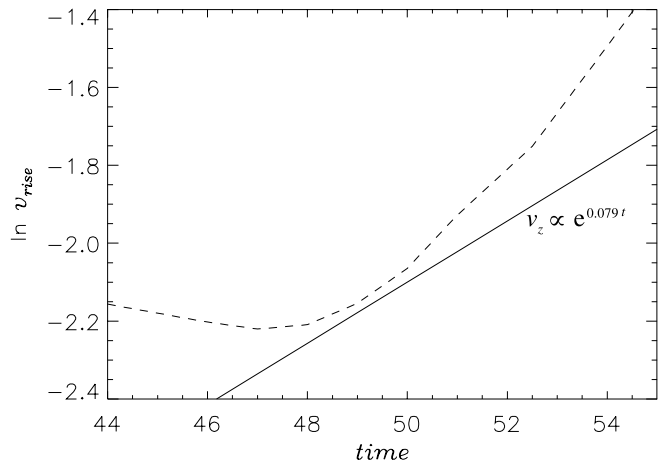
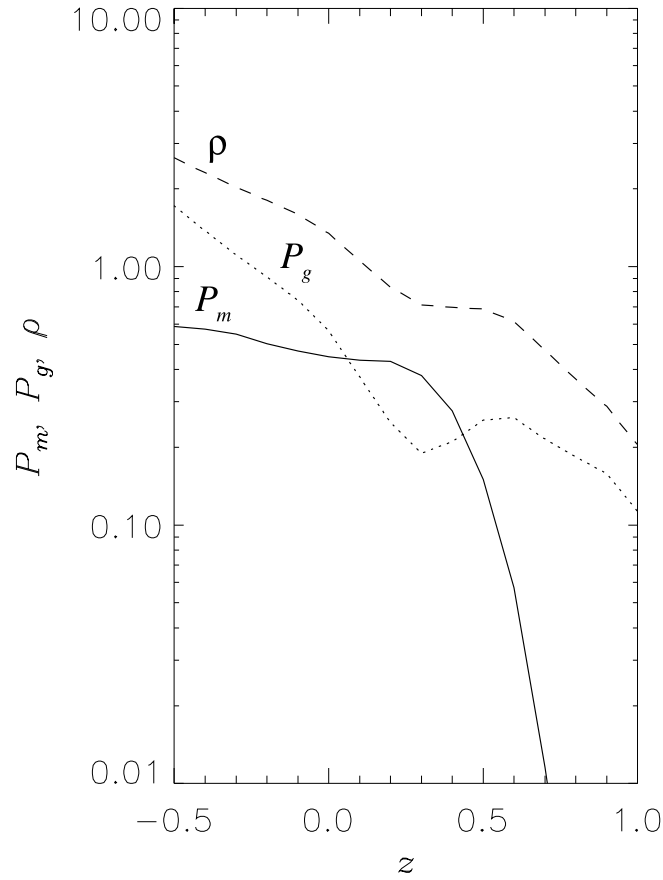
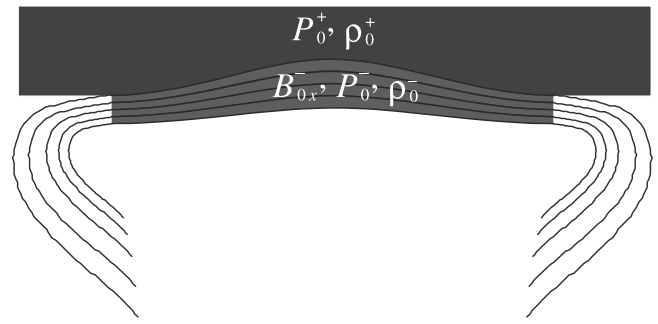


FIG. 6.—*Top*: Schematic illustration of the contact surface between the flattened flux tube (magnetic layer) and the photospheric layer. The physical quantities over the contact surface are shown by the plus sign superscript, and the quantities under the surface are shown by the minus sign subscript. *Middle*: Distributions of magnetic pressure (solid line), gas pressure (dotted line), and gas density (dashed line) along the  $z$ -axis at  $t = 50$  for model T. *Bottom*: Time variation of the Lagrangian velocity of A (dashed line). A solid line shows the velocity development provided by the linear stability analysis for the Rayleigh-Taylor instability.

where  $\omega$ ,  $g$ ,  $k_x$ ,  $\rho_0^+$ ,  $\rho_0^-$ , and  $B_{0x}^-$  are the angular frequency, gravitational acceleration,  $x$ -component of the wavenumber, gas density over the contact surface, gas density under the surface, and  $x$ -component of the magnetic field under the surface, respectively. (If the same directional magnetic field also exists over the contact surface, the second term on the right-hand side of eq. [20] is then multiplied by 2; see Priest 1982, for example.) When we assume that the temperature does not change across the contact surface, equation (20) is then rewritten as follows:

$$\omega^2 = \frac{2\pi}{2\beta_0^- + 1} \left( -\frac{g}{\lambda} + 4\pi \frac{C_A^2}{\lambda^2} \right), \quad (21)$$

where  $\beta_0^- \equiv 8\pi p_0^- / (B_{0x}^-)^2$ ,  $\lambda \equiv k_x / (2\pi)$ , and  $C_A^2 \equiv p_0^+ / \rho_0^+ = p_0^- / \rho_0^-$ , the first of which is the plasma beta under the contact surface, the second is the wavelength, and the last is the isothermal sound velocity. In this derivation, we use the condition of pressure equilibrium at the contact surface, expressed as

$$p_0^+ = p_0^- + \frac{B_{0x}^{-2}}{8\pi}. \quad (22)$$

Equation (21) means that the instability occurs when the wavelength of the undulating magnetic layer is over the critical wavelength  $\lambda_c \equiv 4\pi C_A^2 g^{-1}$ , which becomes 6.28 with  $C_A = (p_p / \rho_p)^{1/2} = 0.775$  and  $g = g_p = 1.2$  at the photospheric level. We also derive  $\beta_0^-$  and  $\lambda$  from the simulation result at  $t = 50$  of model T, the former of which is calculated at the point where the density deficit is maximum inside the magnetic layer, and the latter is derived by means of Fourier analysis of the photospheric distribution of the normal component of the magnetic field. The result is  $\beta_0^- = 0.501$  and  $\lambda = 6.35$ , which suggests that the instability can occur with the growth rate  $i\omega = 0.079$ . The velocity development of this growth rate is shown by a solid line in Figure 6c, which is a close-up view ( $44 \leq t \leq 55$ ) of Figure 3b except that the vertical axis is logarithmically scaled. This figure indicates that the simulation case (*dashed line*) develops at the predicted growth rate around  $t = 50$ .

#### 3.1.4. Phase IV ( $t \geq 55$ )

The magnetic layer emerging through the photosphere by the Rayleigh-Taylor instability begins to expand if the surrounding gas pressure is too weak to counteract the magnetic pressure of the emerging layer (see Fig. 6b). As it expands, the undulation of the magnetic layer causes plasma to flow down from inside the layer, which makes this layer lighter and lighter (see Fig. 2d). After the light layer rises, then the underlying magnetic layer also starts rising because the downward magnetic pressure of the overlying layer decreases. In this way, a large amount of the magnetic field initially stored under the photosphere eventually emerges into the atmosphere (Fig. 2e or 2f), which is known as the Parker instability (Parker 1966).

The nonlinear evolution of emerging magnetic field in the Sun induced by the Parker instability has been thoroughly studied by Shibata and his colleagues. The most prominent feature of the nonlinear phase is that the expansion of the magnetic field proceeds self-similarly (see Figs. 7a–7c). Figures 7a–7c show the distributions of the vertical component of velocity, gas density, and horizontal magnetic field along the  $z$ -axis at three times ( $t = 61, 63, \text{ and } 65$ ). This kind of similarity is also found in some one-dimensional nonsteady gas flows, such as a flow in a shock tube. Shibata et al. (1989) compared the effect of the magnetic pressure with other effects of the gravity, gas pressure, and magnetic tension at the midpoint of an expanding magnetic layer, finding that the former effect is far superior to the other three effects in the early nonlinear phase. This means that the expansion in this phase proceeds like what we could see in a shock tube where an excess of magnetic pressure exists at one side of the shock tube, except that the gas is forced to do the one-dimensional motion in the shock tube. The increased mobility of gas with the multidimensional motions in an expanding magnetic layer compared to a shock tube causes the difference in the distributions of physical quantities behind the propagating shock wave. These distributions are uniform in a shock tube, but nonuniform distributions appear in an expanding magnetic layer. Shibata et al. (1989) analytically solved quasi-one-dimensional MHD equations that include the effect of a plasma sliding down along the magnetic layer. They consequently derived the following relations on the distributions behind the shock wave:

$$v_z \sim \omega_n z, \quad \rho \propto z^{-4}, \quad B_x \propto z^{-1}. \quad (23)$$

Here  $\omega_n$  represents the growth rate in the nonlinear phase, given by

$$\omega_n \sim \frac{1}{2} \omega_l \simeq 0.1(1 + 2\beta_*)^{-1/2} \frac{C_S}{\Lambda}, \quad (24)$$

where  $\omega_l$ ,  $\beta_*$ ,  $C_S$ , and  $\Lambda$  are the linear growth rate, plasma beta, adiabatic sound velocity, and pressure scale height in the magnetic layer (Tajima & Shibata 1997). In the present study, these values are  $\omega_n = 0.21$ ,  $\beta_* = 0.501$ ,  $C_S = 0.652$ , and  $\Lambda = 0.222$ , calculated from the simulation result at  $t = 50$  of model T. The velocity-height relation based on this growth rate is overplotted in Figure 7a (*solid line*). In Figures 7b and 7c, we also draw solid lines to represent the other relations given by equation (23).

We now briefly explain the relations in equation (23). The first relation  $v_z \propto z$  tells us that the rise velocity of a plasma increases exponentially with time in the Lagrangian frame (from  $dz/dt = \omega_n z$  we obtain  $z \propto e^{\omega_n t}$ ). According to Tajima & Shibata (1997), this is because the downflow speed of a plasma from an expanding magnetic layer also has the exponential time dependence (increasing) in the Lagrangian frame. The remaining relations,  $\rho \propto z^{-4}$  and  $B_x \propto z^{-1}$ , are derived from that velocity relation above assuming that the density has the exponential time dependence (decreasing) in the Lagrangian frame, which consequently presents the steady solutions of expanding magnetic layer in the Eulerian frame.

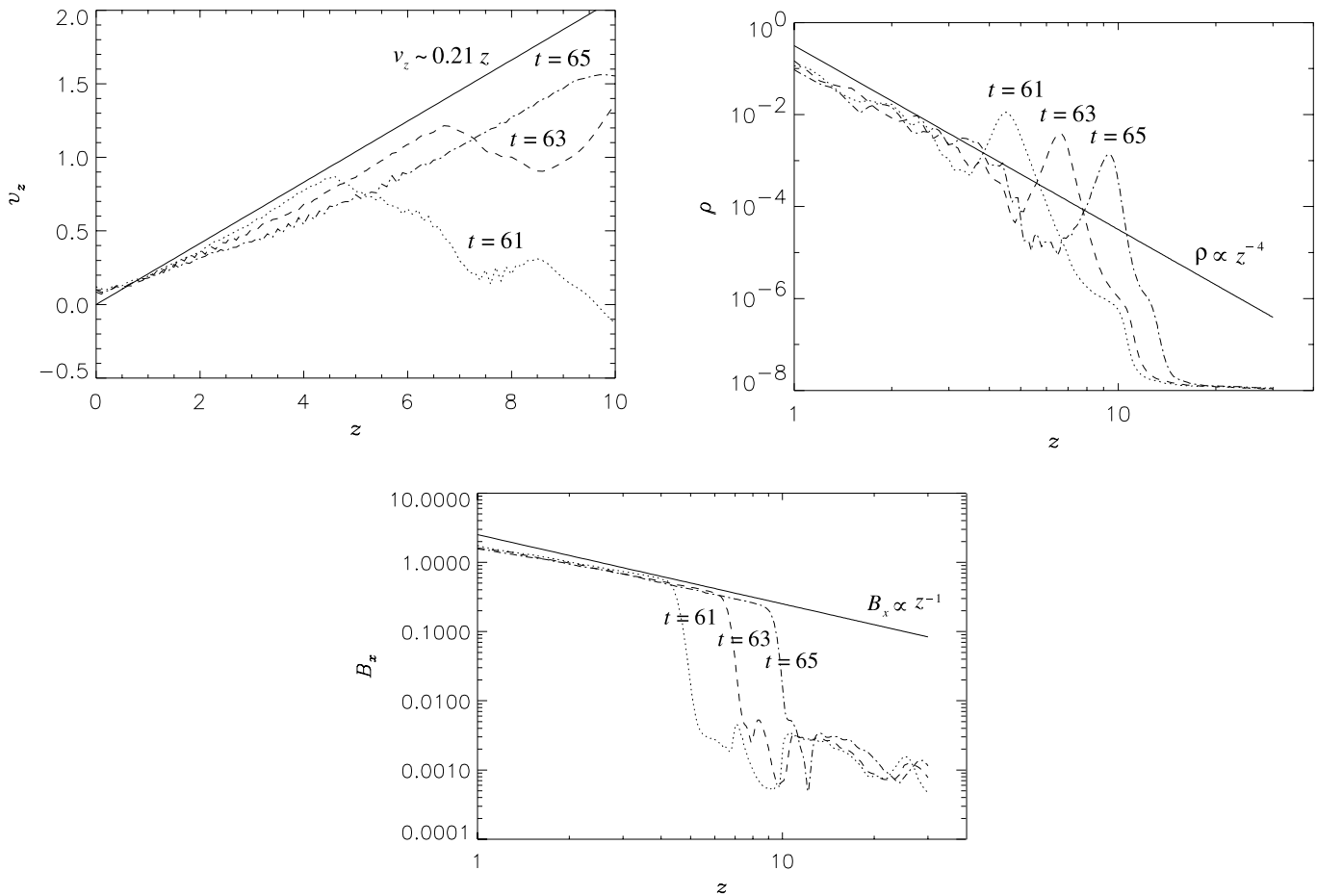


FIG. 7.—*Top*: Distribution of the vertical component of velocity along the  $z$ -axis for model T. Dotted, dashed, and dot-dashed lines represent the distribution at  $t = 61, 63,$  and  $65$ , respectively. A solid line shows the velocity-height relation provided by the nonlinear analysis for the Parker instability. *Middle*: Distribution of gas density along the  $z$ -axis for model T. The notation of lines is the same as in the top panel. *Bottom*: Distribution of the horizontal component of magnetic field along the  $z$ -axis for model T. The notation of lines is the same as in the top panel.

### 3.2. Energetics

In order to study the state of magnetic structure in the atmosphere, one of the useful ways is to estimate the magnetic energy stored in that structure and compare it with the potential energy derived from the same boundary conditions as the structure has. We here put a boundary at  $z = 0$ , the photospheric level, and calculate the magnetic energy stored in the tube over this boundary (we hereafter use the term “magnetic arcade” to represent the area of the tube above the photosphere). We also calculate the magnetic energy of the potential field, whose normal component at the boundary has the same distribution as the tube’s field. The detailed procedure for calculating the potential energy is given in the Appendix.

Figure 8 shows the variation of magnetic energies with time, where these energies are calculated in half of the total simulation domain by assuming symmetry with respect to the  $z$ -axis. The solid line indicates the magnetic energy stored in the arcade, while the dotted line indicates the potential energy. As for the energetics of magnetic structure over the photosphere, there are two main processes that affect the stored magnetic energy: the emergence of subphotospheric magnetic field and the expansion of magnetic structure. The former enhances the stored magnetic energy while the latter reduces it. Looking at Figure 8, we find the rapid development of the magnetic energy of the arcade in the early stage, which indicates that the former effect is stronger than the latter effect. We also find that the rate of increase of the potential energy becomes large with time, which suggests that the flux emergence is active in that stage. On the other hand, the emergence process becomes weak after  $t = 60$  as the expansion effect of magnetic arcade becomes prominent. Both the increase of the energy stored in the arcade and the increase of potential energy slow down with time, and furthermore the difference between these two energies becomes smaller with time. This implies that the magnetic arcade comes close to the potential field as it expands. The decline of flux emergence is also visible in Figures 3a and 3b, where the evolution of tracers B and C (initially located at the center and bottom of the tube) shows no strong rise motion in contrast to the tracer A (initially located at the top of the tube).

The suppression of flux emergence in the late phase can be understood by considering the critical wavelength for the Parker instability:

$$\lambda \geq \lambda_p \sim 10\Lambda \quad \text{for } \beta \sim 1, \quad (25)$$

where  $\lambda$ ,  $\lambda_p$ , and  $\Lambda$  are the wavelength of the undulating magnetic layer, critical wavelength, and local pressure scale height, respectively (Parker 1979). This condition means that too sharp an undulation provides a strong tension force to suppress the

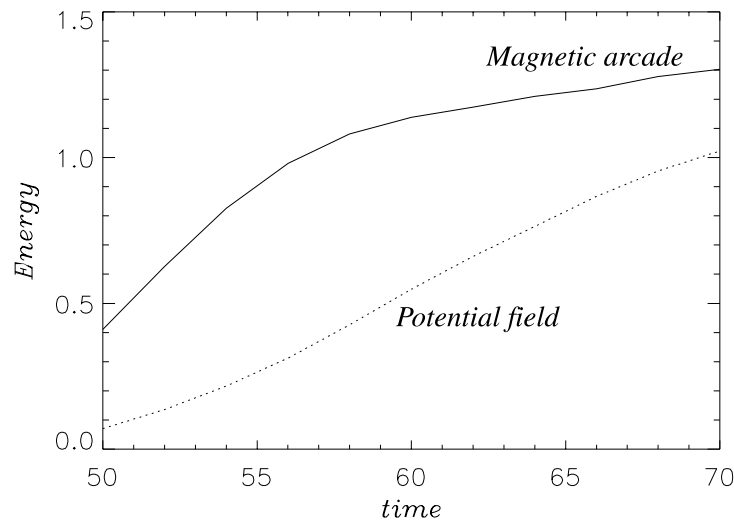


FIG. 8.—Time variation of magnetic energies. A solid line represents the energy stored in the magnetic arcade, and a dotted line represents the potential energy.

instability. Examining the field line configuration around the photosphere in Figure 2*f*, we found that younger emerging field lines have a smaller undulation wavelength. In the present study  $\Lambda$  is around 0.5 (see Table 1) so that it becomes impossible for some late emerging field lines to satisfy the condition given by equation (25). For such field lines, the downward tension force works effectively to suppress their rise motion. Accordingly, although the upper part of the tube emerges and expands into the atmosphere, a significant amount of magnetic field in the tube still remains under the photosphere.

### 3.3. Model Dependences

#### 3.3.1. Strength of Magnetic Field

In order to see how the strength of axial magnetic field affects the tube dynamics, we make a comparison between model WB and model T. Figure 9 shows the motion of the top of the tube with time for these two models, where solid and dotted lines represent models T and WB, respectively. From this figure it is found that both models have a similar evolution, though their timescales are different. The tube of model WB, which has a weaker axial magnetic field, rises a little more slowly through the convection zone than the tube of model T, and the emergence and the following expansion processes of model WB are quite delayed compared to those of model T. That is to say, the difference in evolution between those models is small in the region where the magnetic pressure is weaker than the gas pressure (large plasma  $\beta$  region), such as the convection zone, but the difference becomes fairly large in the magnetic-dominant region.

#### 3.3.2. Radius of the Tube

We use models WB, Sr, and Lr to see the effect of the radius of the tube on the evolution. The tubes in these models have the same axial magnetic field at the tube center but different radii. We again pay attention to the top part of the tube and follow the evolution of this. Figure 10 shows the result for these three models, where solid, dotted, and dashed lines represent models

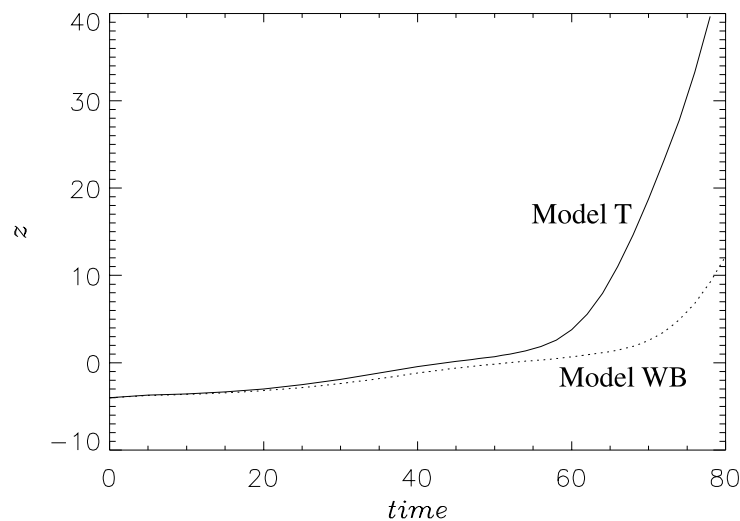


FIG. 9.—Height-time relation of the top of the flux tube. Solid and dotted lines represent models T and WB, respectively.

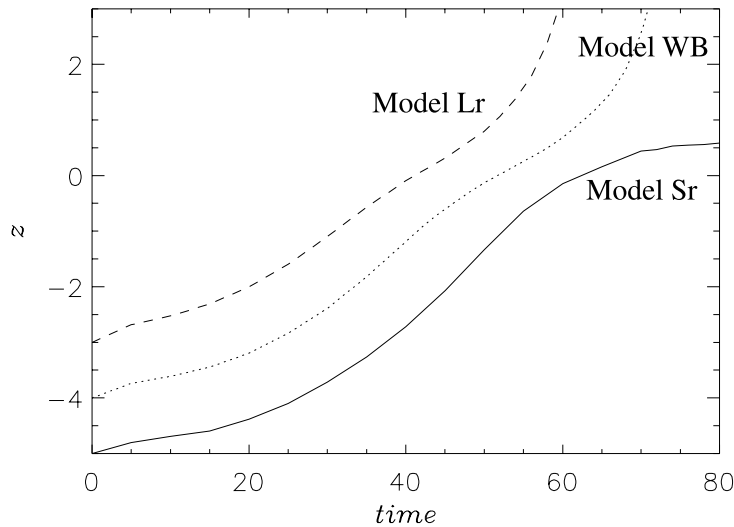


FIG. 10.—Height-time relation of the top of the flux tube. Solid, dotted, and dashed lines represent models Sr, WB, and Lr, respectively.

Sr, WB, and Lr, respectively. This figure shows that the tubes with larger radius (models WB and Lr) evolve in the same way except for their timescales, although model Sr has a distinct pattern of evolution from the first two models. Model Sr shows an evolution in the convection zone similar to the other models; however, it does not have any dynamical expansion phase in the atmosphere. In other words, the tube of model Sr is almost in equilibrium vertically after it reaches the photosphere, as Figures 11a–11d show. These figures indicate that the tube rises through the convection zone and then suffers from a severe flattening, which enhances the undulation wavelength of the magnetic layer formed under the photosphere. Figure 12a shows the photospheric distribution of the normal component of magnetic field at several times for model Sr ( $t = 60$ , solid line;  $t = 65$ , dotted line;  $t = 70$ , dashed line;  $t = 74$ , dot-dashed line;  $t = 78$ , three-dot-dashed line). From this figure it is found that the wavelength of the undulating magnetic layer increases smoothly with time at first, but later such increase saturates at some level. This is more clearly seen in Figure 12b, where the wavelengths derived by means of Fourier analysis are plotted against time along with a horizontal line to represent the critical wavelength for the Rayleigh-Taylor instability (see § 3.1.3). This figure shows that the flattening of the tube proceeds until the undulation wavelength reaches the critical wavelength,

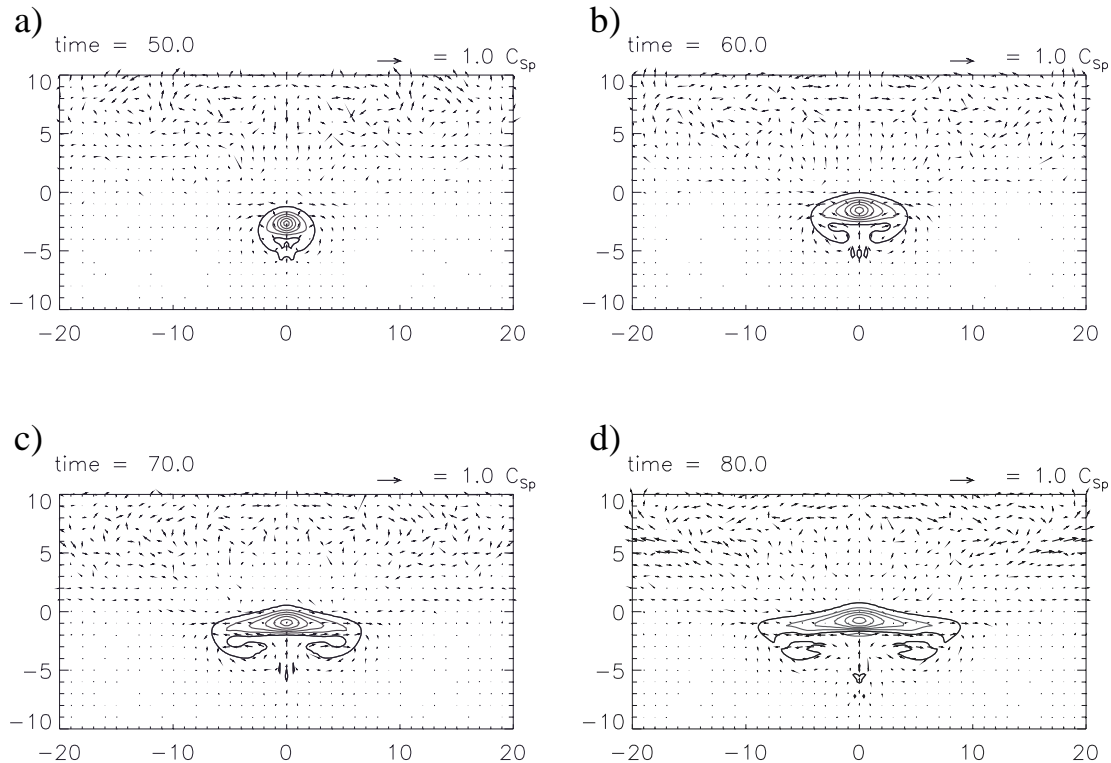


FIG. 11.—Two-dimensional view graphs showing the evolution of the flux tube for model Sr. (a)  $t = 50$ ; (b)  $t = 60$ ; (c)  $t = 70$ ; (d)  $t = 80$ . A black contour line and gray contour lines show the boundary and the internal magnetic field lines of the tube, while arrows represent the flow velocity field.

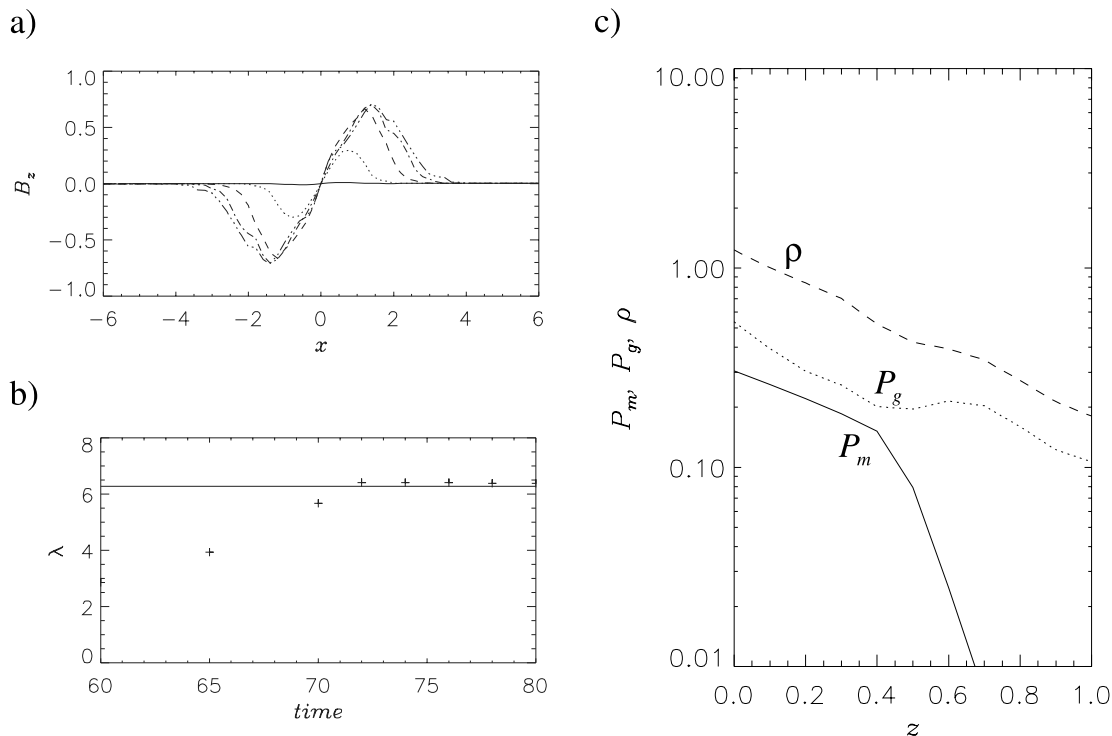


FIG. 12.—(a) Distribution of the normal component of magnetic field along the  $x$ -axis for model Sr. Solid, dotted, dashed, dot-dashed, and three-dot-dashed lines represent the distribution at  $t = 60, 65, 70, 74,$  and  $78,$  respectively. (b) Time variation of the wavelength of the undulating magnetic layer for model Sr. Crosses show the wavelength at  $t = 60, 65, 70, 72, 74, 76, 78,$  and  $80.$  A horizontal line shows the critical wavelength for the Rayleigh-Taylor instability. (c) Distributions of magnetic pressure (solid line), gas pressure (dotted line), and gas density (dashed line) along the  $z$ -axis at  $t = 76$  for model Sr.

although the excess over the critical value does not lead to the following expansion in this case. The reason of no dynamical expansion phase can be understood when we look at Figure 12c, where the vertical distributions of the gas pressure, density, and magnetic pressure along the symmetric axis for model Sr are shown. Compared to Figure 6b, this figure shows some similar features, such as the depressions of the gas density and pressure inside the tube, but it also shows that the magnetic pressure is weaker than the gas pressure in that depression area. This means that the top part of the tube cannot make a strong expansion in model Sr because the surrounding gas pressure is so strong as to suppress such a dynamical process.

#### 4. DISCUSSION

In this section we discuss the relation between the results presented above and some observational results. We focus on two solar phenomena. One is the birth of emerging flux tubes, and the other is the formation of filaments. These phenomena have now been observed extensively by various sophisticated observational instruments. In the following, based on fruitful observational results, we make a detailed interpretation of our results and discuss the physical processes expected to work in those phenomena.

##### 4.1. Birth of Emerging Flux Tubes

First, let me show what one can observe above the photosphere, based on the results of the 2.5-dimensional simulations. Figures 13a–13d are three-dimensional view graphs of a magnetic arcade appearing over the photosphere, where black lines and a gray-scale map represent the magnetic field lines and the normal component of photospheric magnetic field, respectively. We draw three loop systems in each view graph, all of which have no difference under the present 2.5-dimensional simulation. This figure shows that the magnetic field lines start emerging with their directions almost transverse to the neutral line in the early stage ( $t = 50$ ), while we can see sheared field lines in some later stages ( $t = 62$  and  $68$ ). This is a typical nature of magnetic arcades observed in the Sun, that is, the inner magnetic field lines of arcade have more sheared structure than the outer field lines (Schmieder et al. 1996). Looking at the gray-scale map, we find that a magnetic belt appears in the photosphere with its width about 6 in the early stage ( $t = 50$ ), which corresponds to about 2 times the size of a granule (1800 km). This size, as we mentioned in § 3.1.3, is related closely to the physical process generated at the contact surface between the tube and the photosphere. As the arcade expands, that magnetic belt increases its width and strength, the latter of which reaches over 600 G in the later stage ( $t = 68$ , over the absolute value of 1.3). Recent observations suggest that the photospheric magnetic field is distributed sporadically over the photosphere and each magnetic element has such a strong magnetic field as is over 1 kG (Solanki 1994). The maximum strength 600 G we obtained here might be enhanced to that level if we took the radiative cooling effect into consideration, which causes the convective collapse at the footpoint of arcade (Spruit 1979; Parker 1979; Nozawa et al. 1992; Takeuchi 1993; Steiner et al. 1998).

We shall now look more closely at the physical process related to these phenomena. Figure 14a is a schematic illustration of the emergence of a flux tube and the associated arcade formation. Although the present simulation is 2.5-dimensional, we here

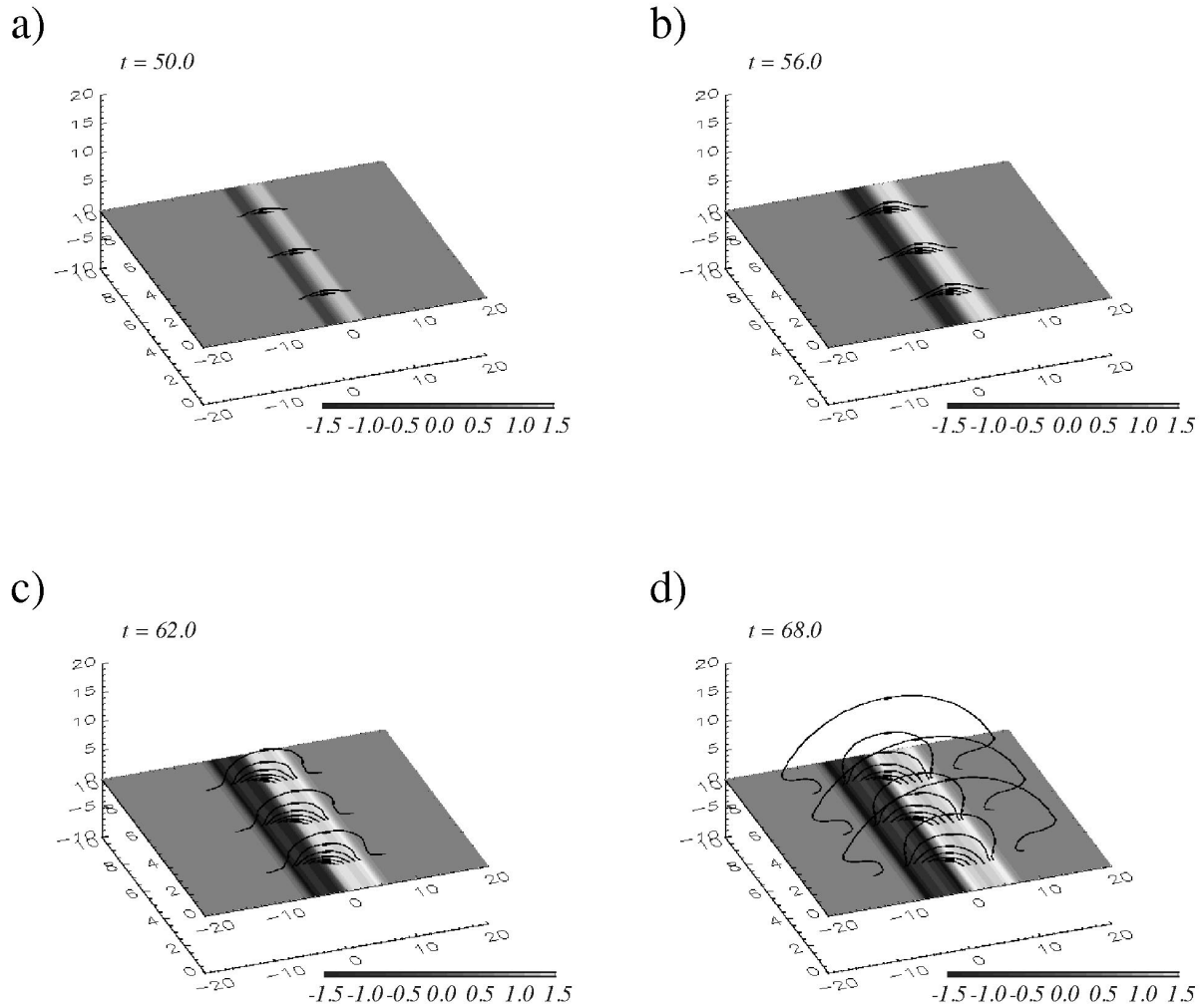


FIG. 13.—Three-dimensional view graph showing the appearance of magnetic arcade for model T. (a)  $t = 50$ ; (b)  $t = 56$ ; (c)  $t = 62$ ; (d)  $t = 68$ . Black curves represent the magnetic field lines, and a gray-scale map located at  $z = 0$  shows the photospheric distribution of the normal component of the magnetic field.

consider a three-dimensional behavior, that is, the tube can undulate along its axis with the cross section deformed. We set the  $y$ -axis along the tube axis and then discuss the Rayleigh-Taylor instability in the more general three-dimensional situation. In the case including the variation along the  $y$ -axis, the dispersion relation of that instability is written as follows:

$$\omega^2 = \frac{1}{2\beta_0 + 1} (-gk + 2C_A^2 k_x^2), \quad (26)$$

where  $k \equiv (k_x^2 + k_y^2)^{1/2}$  and the remaining characters are the same as in § 3.1.3. We then define  $f(k_x, k_y) \equiv -(k_x^2 + k_y^2)^{1/2} + 2C_A^2 g^{-1} k_x^2$  and investigate the change of this as a function of  $k_x$  and  $k_y$ . The result is shown in Figure 14b, where contours of  $f(k_x, k_y)$  are displayed in solid lines. This figure shows that the instability area [ $f(k_x, k_y) < 0$ ] becomes large as  $k_y$  increases, that is, when  $k_y = 0$  (corresponding to the 2.5-dimensional case) the instability occurs in the range of  $0 < k_x < (2C_A^2)^{-1}g$ , while for the case of  $k_y > 0$  the instability range of  $k_x$  is expressed as

$$0 < k_x < k_C, \quad (27)$$

where

$$k_C = \frac{\sqrt{2 + 2\sqrt{1 + 4(2C_A^2 g^{-1} k_y)^2}}}{4C_A^2} g. \quad (28)$$

Equation (28) shows that  $k_C$  starts with  $(2C_A^2)^{-1}g$  and increases monotonically as  $k_y$  increases from 0 to infinite. The analysis above suggests that an arcade can appear with smaller width when the emergence part of the tube undulates more strongly along its axis.

The latest observational instruments enable us to see closely the very dynamical nature of various fine structures in the Sun. For example, the Michelson Doppler Imager (MDI) on board the *Solar and Heliospheric Observatory (SOHO)* provides us with interesting movies of tiny magnetic poles moving actively in the photosphere, which shows a very intermittent nature of those magnetic poles (see Fig. 15a). High-performance ground-based solar telescopes also make it possible to see tiny arch

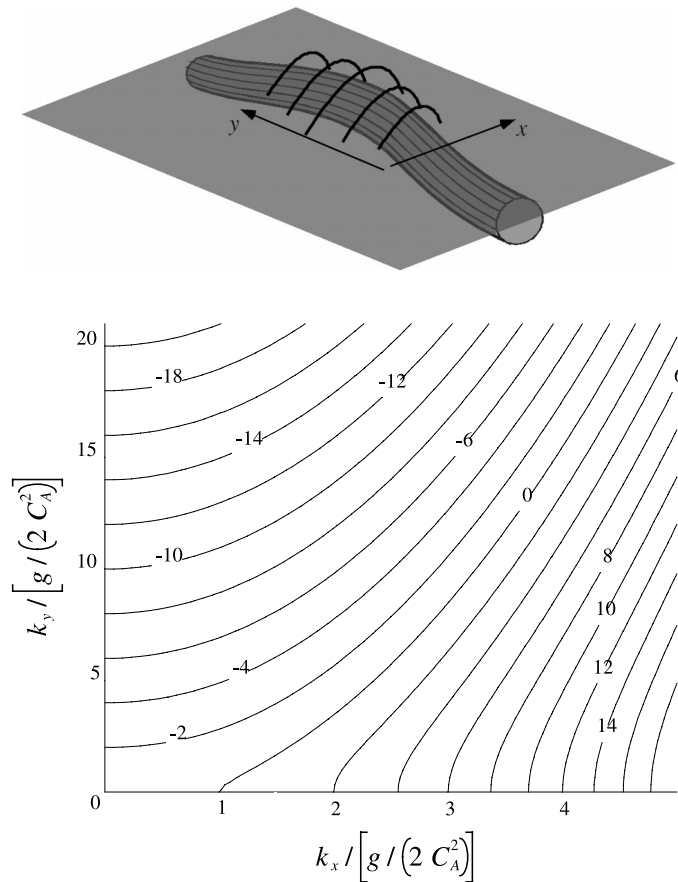
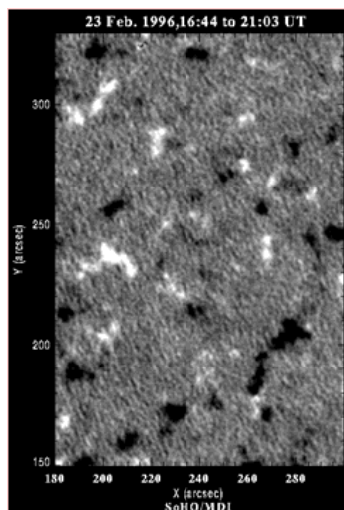


FIG. 14.—*Top*: Schematic illustration of emergence of the flux tube and arcade formation. *Bottom*: Contour plot of  $f(k_x, k_y)$ . Both axes are scaled by  $g/(2C_A^2)$ .

filament systems (AFSs) in the solar surface, some of which survive for a long period of time and later develop into major active regions (see Fig. 15b). We do not yet have a clear understanding of what causes the difference in the evolution of emerging flux tubes, though the present study suggests that not all of the emerging flux tubes can expand to form major structures in the atmosphere. In order to come to the atmosphere, flux tubes rising through the convection zone have to satisfy the emergence condition at the contact surface between the tube and the photosphere. Furthermore, even if they satisfy this condition, flux tubes cannot expand dynamically when the magnetic pressure of the emergence part is too weak compared

a)



b)

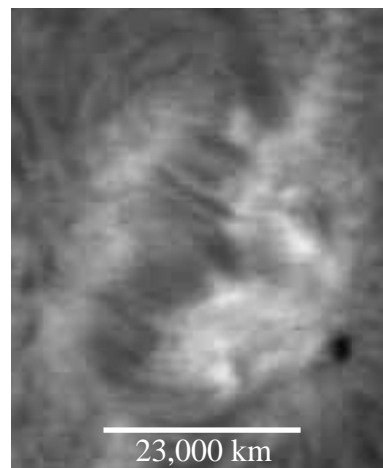


FIG. 15.—(a) Photospheric distribution of magnetic poles. Courtesy of *SOHO*/MDI consortium. *SOHO* is a project of international cooperation between ESA and NASA. (b) Example of an arch filament system observed in  $H\alpha$ . The length of the white line at the lower part of the figure corresponds to  $32''$  (23,000 km). Courtesy of Dr. K. Yoshimura at Hida Observatory.

to the surrounding gas pressure (see § 3.3.2). For such weak tubes, the emergence part over the photosphere could be easily controlled by severe photospheric motions so that it cannot survive long, showing an intermittent behavior. This is, however, only a rough conjecture at present. In order to make this firm, it is necessary to know more detailed behavior of emerging flux tubes in their birth stages, which should be one of the most important targets of upcoming observational missions.

#### 4.2. Filament Formation

Next, we focus on the formation of filaments that are not only prominent cool matters floating in the hot corona but also the important objects seeming to be connected closely with the energy source of the surrounding magnetic structure (Amari et al. 2000). There are mainly two kinds of filaments. One is that a plasma is condensed on top of a magnetic arcade to form a dense structure (normal polarity filaments). On the other hand, a plasma cools down inside a twisted flux rope in the corona, forming a filament at the bottom of that flux rope (inverse polarity filaments). There are some ideas on the origin of the flux rope surrounding a filament plasma. It may originate from a flux tube in the convection zone (Low 1994), or it may be formed in the atmosphere by magnetic reconnection (van Ballegoijen & Martens 1989). Here we consider the formation of inverse polarity filaments from the viewpoint of a flux tube rising from the subphotosphere. The first step is to lift a flux tube over the photosphere; however, as mentioned earlier, since the emergence process is suppressed more strongly by magnetic tension force at the later phase, we artificially enhance the buoyancy effect by reducing the matter inside the tube. We carry this out for model T after  $t = 60$  and investigate the following evolution. The result is shown in Figures 16a–16c, where the density-reduced area is circled with a black thick line inside the tube (this line corresponds to a certain contour line of magnetic flux). Actually, we can expect that the density reduction inside the tube happens in some three-dimensional situations. For example, the undulation of the tube along its axis can cause matter to flow down along the axis, decreasing the gas density at the crest of the undulating tube. Since the 2.5-dimensional simulation cannot reproduce this process precisely, our current attention is paid not to the detailed formation process of filaments but to the energetics related to the emergence of the flux tube.

Figure 16d shows the time variation of magnetic energies, similar to Figure 8. Solid and dotted lines represent the energy stored in the arcade and the potential energy, respectively. The evolution in the early phase ( $t \leq 60$ ) is completely the same as in Figure 8, though the latter phase is affected strongly by the enhanced buoyancy. This effect is clearly seen in the abrupt increase of energy at  $t = 62$ , which is caused by the strong injection of new magnetic fluxes to the atmosphere. The increase of energy, however, stops around  $t = 70$  when the center of the tube goes over the photosphere, and after that both energies start decreasing. Such energy decreases are explained as follows. The magnetic energy stored in the arcade is supplied by the emerging effect of the magnetic field, which later weakens by magnetic tension force. This implies that the energy input through the emergence is eventually smaller than the energy output through the expansion of the magnetic arcade. Further-

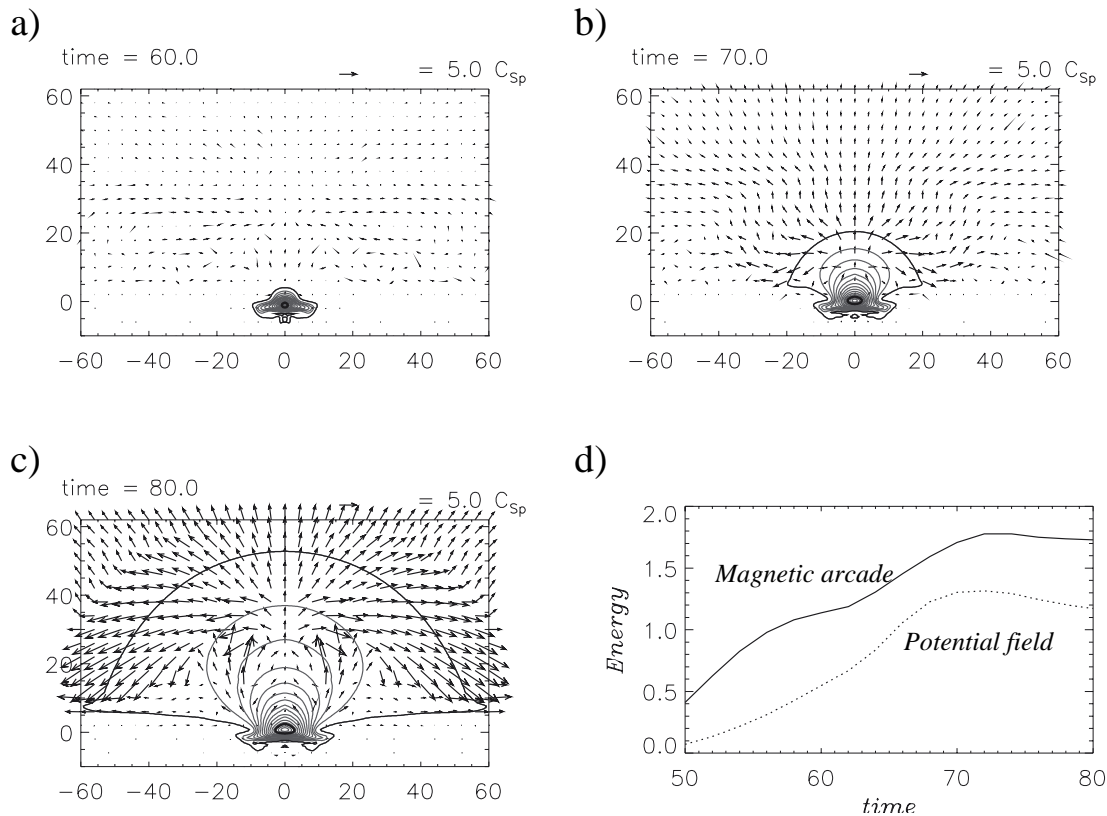


FIG. 16.—Two-dimensional view graphs showing the evolution of the flux tube for model T (enhanced buoyancy case). (a)  $t = 60$ ; (b)  $t = 70$ ; (c)  $t = 80$ . A black contour line, gray contour lines, and arrows show the boundary of the tube, magnetic field lines, and flow velocity field, respectively. The area surrounded by a thick black circle inside the tube indicates the density-reduced area. (d) Time variation of magnetic energies. A solid line represents the energy stored in the magnetic arcade, and a dotted line represents the potential energy.

more, the strong magnetic field concentrates around the tube center so that the energy input through the emergence becomes less effective after the tube center goes over the photosphere. On the other hand, the decrease of the potential energy is explained in a different way. Since the potential energy only depends on the distribution of the magnetic field at the boundary, the decrease of this energy means that the boundary field weakens through the emergence. This can be more easily understood if we imagine the emergence of a flux tube with purely circular cross section. For such a flux tube, the field strength across the photosphere increases as the tube center rises close to the photosphere, though once the center goes over the photosphere, the field strength decreases as the emergence proceeds. The cross section of the tube is actually far from the circular shape in the simulation; however, the same consideration as mentioned above holds true for the decrement of the potential energy after the tube center goes over the photosphere.

Let us devote a little more space to discussing the free energy stored in the magnetic arcade. If we regard this as the difference between the magnetic energy stored in the arcade and the potential energy, Figure 16d shows that there are two periods during which the free energy increases. The first is the early stage ( $0 \leq t \leq 60$ ) when the tube starts emerging, and the next is the later stage ( $70 \leq t \leq 80$ ) after the tube center goes over the photosphere. The point to be noticed is that the free energy is used in different ways in these two stages. That is to say, the free energy gained in the early stage is released naturally through the expansion process so that the energy stored in the arcade approaches the potential energy with time (see Fig. 8). On the other hand, the magnetic arcade gains more free energy in the later stage by including a helical magnetic structure within the arcade. Since helical magnetic fields generate currents, the energy level of the arcade becomes higher than the potential energy level. The free energy provided by those helical fields is not completely consumed by the expansion process. In other words, the free energy gained in the early stage is doomed to be lost as the magnetic arcade expands, though part of the later storage of free energy remains in the arcade as long as the helical structure exists. From the observational viewpoint, the free energy gained in the early stage induces strong mass motions associated with AFSs, while the later storage probably gives birth to various explosive phenomena observed in the well-developed phase followed by the early expansion phase, such as flares, filament eruptions, and so on. Precisely speaking, the free energy gained in the early stage cannot be lost only by the expansion process if the photospheric boundary field has a sheared structure. In this case, another process such as the footpoint motion of the arcade is needed to reduce the energy to the potential level. However, as far as strongly twisted flux tubes are concerned, the photospheric boundary field is little sheared before the tube center emerges because strong axial fields are concentrated in the very small area around the tube center. On the contrary, the storage in the later stage cannot be lost completely even if the photospheric boundary field becomes shearless.

Finally, let us briefly mention the limitation of the present study. In spite of the effort to lift the tube center, the magnetic tension force is so strong that the center rises slightly, which is far from reaching the corona to form a filament. One possibility to break this situation is suggested by the result of Krall et al. (1998), which shows the effect of external magnetic fields on the dynamics of the buoyant flux tube. In the present study, external magnetic fields are so weak that they have little effect on the dynamics of the emerging flux tube; however, the appropriately set external fields might make a significant contribution to the formation of the coronal flux tube. Another possibility comes from three-dimensional effects. For example, the undulation of the tube along its axis causes the kink instability, which induces the rise motion of the crest of the undulating tube. The kink instability also changes the side view of an arcade into a fanlike shape, which can often be observed on the Sun. If this process indeed happens, we then come to the conclusion that a three-dimensional process is needed to connect between the initial and final states, even if both states are almost 2.5-dimensional.

## 5. SUMMARY

We here summarize the dynamics of emerging flux tubes by looking at the time variation of the vertical velocity along the symmetric axis. Figure 17 is a three-dimensional view graph of  $v_z(0, z, t)$ -distribution, where the distribution of the vertical velocity along the symmetric axis is shown at some selected times. Since this view graph well reflects the dynamical situation in all the evolutionary stages, we briefly mention the features of each stage by referring to this figure. First, it is found that the unidirectional rise motion persists in the convection layer ( $z < 0$ ). This comes from the fact that this layer is convectively unstable. The tube then experiences buoyancy breaking when it reaches the convectively stable photosphere ( $z = 0$ ). The motion is then changed into the oscillatory mode, which propagates toward the upper atmosphere. From the photosphere to the corona, the temperature increases rapidly and the gas density decreases significantly. The former effect enhances the sound velocity, making the wavelength longer, and the latter effect increases the amplitude of velocity. These behaviors can be seen in the distribution at  $t = 25$ .

The flux tube moves together with the plasma flow because the complete coupling between the magnetic field and the plasma is assumed in the present simulation. In the convection zone the flux tube rises by magnetic buoyancy, which is also supported smoothly by the unidirectional rise motion of the plasma. As to the cross section of the tube, there is no strong change during the rise phase in the convection zone, though we can see a significant flattening when the top of the tube reaches the photosphere. As opposed to the plasma in the convection zone, the photospheric plasma inhibits the smooth rise of the tube by its oscillatory motion, which reduces the rise velocity of the top of the tube relative to the other parts of the tube remaining in the convection zone ( $t = 45$ ). The difference in rise velocity generated inside the tube changes the cross section from the circle to the flat shape.

In this flattening process, a horizontal magnetic layer is locally formed under the contact surface between the tube and the photosphere. As the flattening proceeds, plasma inside this layer is squeezed out to both sides of the layer, making the layer lighter than the overlying layer. In this way, the contact surface becomes Rayleigh-Taylor unstable, which finally causes the magnetic layer to emerge over the surface. If the magnetic pressure of the emerging part is sufficiently stronger than the surrounding gas pressure, the magnetic layer then starts expanding toward the upper atmosphere, which is shown by the increase of the rise velocity just over  $z = 0$  at  $t = 58$ .

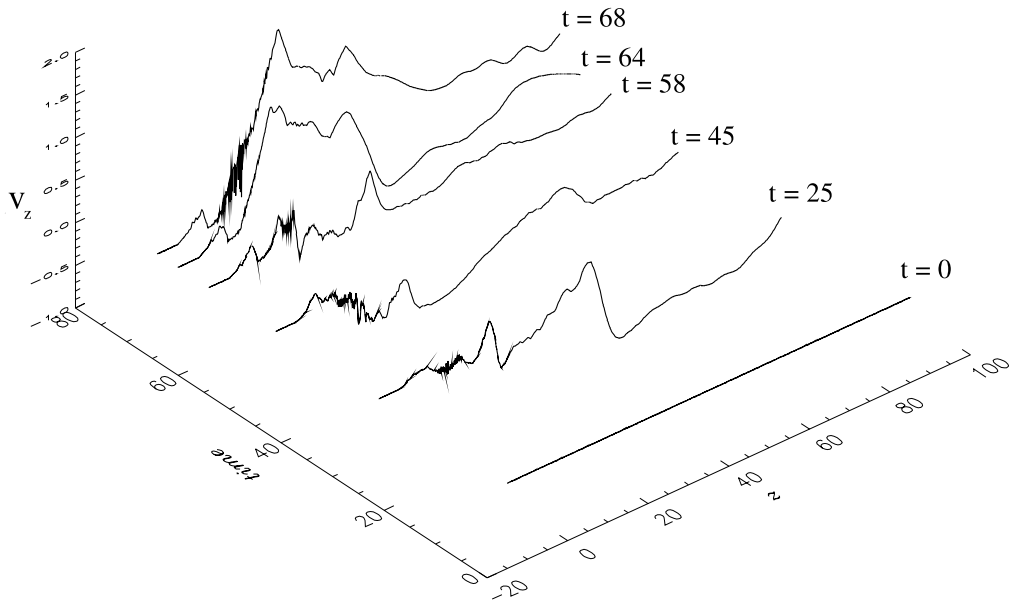


FIG. 17.—Three-dimensional view graph of the distribution of the vertical velocity as a function of  $z$  and  $t$  for Model T

The evolution of the magnetic layer expanding into the atmosphere is characterized by self-similar behavior, that is, the dependence of rise velocity on the height does not change with time. That dependence is given by  $v_z \propto z$ , which is reproduced by the slope over  $z = 0$  at  $t = 64$ . From the viewpoint of energetics, the expansion means that a magnetic arcade formed over the photosphere approaches lower energy state, where the released magnetic energy is used to cause strong mass motions observed as, for example, downflows in AFSs.

The emergence of magnetic field does not bring the entire flux tube above the photosphere because the undulation wavelength of magnetic field lines becomes small in the later phases. Then the magnetic layer becomes stable to the Parker instability, which means that the rise motion changes to oscillatory mode. This can be seen in the lower part of the slope at  $t = 68$ . In the present study, the emergence of the tube center is inhibited by the effect of magnetic tension force, though that process probably plays an important role in forming a filament as well as providing the energy source for later explosive phenomena. We expect that the effects of external magnetic fields and three-dimensionality may break through this deadlock, which is the target of our future study.

I deeply appreciate fruitful discussions with the attendants at the summer seminar held at Hida Observatory in 1999. I also thank an anonymous referee for well-pointed suggestions. Other thanks are due to Dr. K. Yoshimura and *SOHO*/MDI consortium for permission to use photographs in this paper. The three-dimensional visualization has been made with the help of the IDL program developed by Dr. T. Yokoyama. The numerical computations have been carried out by using NEC SX-4 at the National Institute of Fusion Science in Japan. This research was supported by AFOSR under grant F49620-00-1-0128.

## APPENDIX

### CALCULATION OF POTENTIAL MAGNETIC FIELD

Here we try to derive the potential field from the photospheric distribution of the normal component of magnetic field. First, we write the potential field as  $\mathbf{B} = -\nabla\psi$ , where  $\psi(x, z)$  is the potential function satisfying the Laplace equation. Then we seek for a solution of this equation under the following boundary conditions:

$$-\frac{\partial\psi}{\partial z}(x, 0) = B_z(x, 0), \quad (\text{A1})$$

$$\psi(l, z) = \psi(-l, z) = 0, \quad (\text{A2})$$

and

$$\psi(x, \infty) = 0, \quad (\text{A3})$$

where  $x = \pm l$  represents the positions of side boundaries (see Fig. 18).

By using the standard method of separation of variables and assuming symmetry with respect to the  $z$ -axis,  $\psi$  is described as follows:

$$\psi(x, z) = \sum_{m=1}^{\infty} b_m \frac{l}{m\pi} \sin\left(\frac{m\pi}{l}x\right) e^{-(m\pi/l)z} \quad (m = 1, 2, \dots), \quad (\text{A4})$$

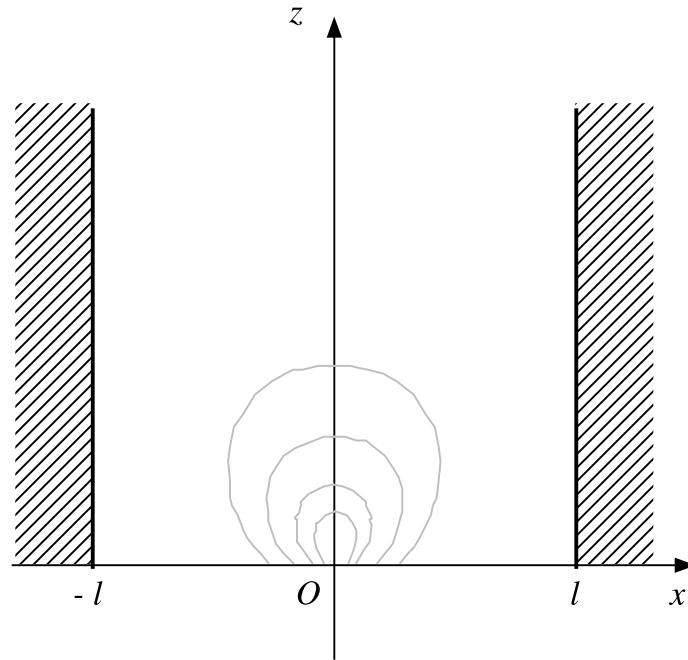


FIG. 18.—Schematic illustration of the calculation domain for the potential field. Light gray curves represent field lines.

where  $b_m (m = 1, 2, \dots)$  are the Fourier coefficients of the normal component of the magnetic field in the photosphere. The explicit form of them is given by

$$b_m = \frac{2}{l} \int_0^l B_z(x, 0) \sin\left(\frac{m\pi}{l} x\right) dx \quad (m = 1, 2, \dots). \tag{A5}$$

In order to obtain a solution with better accuracy, we have to make both  $l$  and the number of Fourier modes larger. Actually, we choose the number of modes as 500, which means that the resolution of the finest mode is  $l/(m\pi) = 100/(500\pi) \sim 0.06$  when we choose  $l = 100$ . This size is comparable to the finest grid size of the present simulation ( $\Delta x = 0.1$ ). Figure 19 shows an example of the fitting by Fourier series.

The potential energy is now calculated as follows:

$$\mathcal{E}_{\text{pot}} = \frac{1}{8\pi} \int_0^\infty \int_0^l (B_x^2 + B_z^2) dx dz = \frac{1}{8\pi} \sum_{m=1}^\infty \frac{b_m^2 l^2}{2m\pi}, \tag{A6}$$

where we used the orthogonal relation among Fourier components.

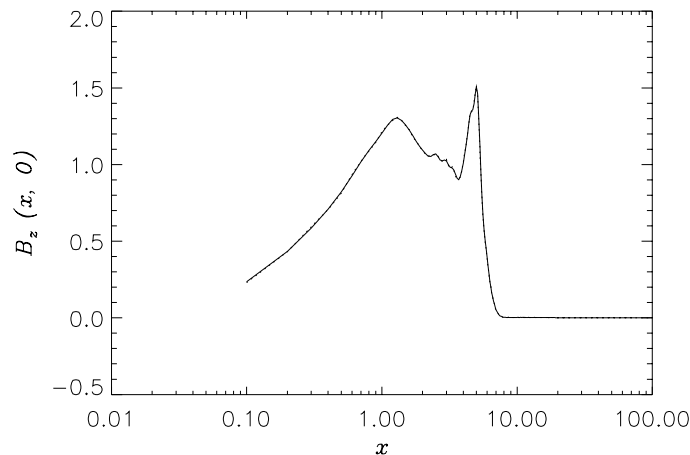


FIG. 19.—Distribution of the normal component of magnetic field along the  $x$ -axis. A dotted line represents the simulation result, while a solid line shows the distribution constructed from Fourier series. Horizontal axis is logarithmically scaled. Since the finest grid size is 0.1 in the present simulation, the minimum value of the  $x$ -coordinate is 0.1.

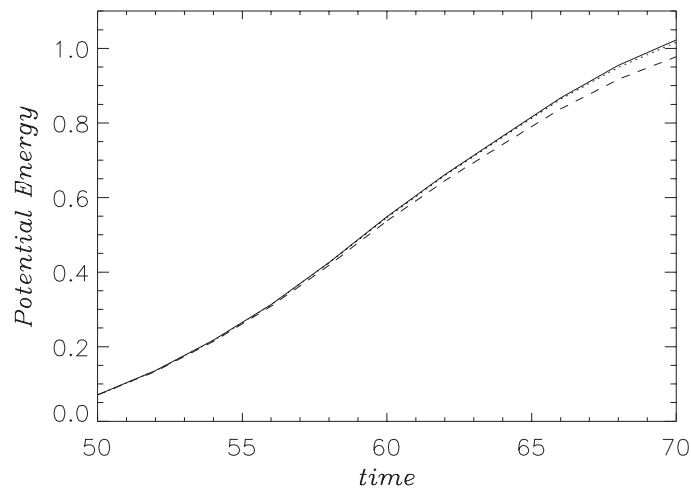


FIG. 20.—Time variation of potential energy. Solid, dotted, and dashed lines represent the cases of  $l = 100$ , 50, and 20, respectively.

As for the position of the side boundary, we should put this farther from the symmetric axis for reducing the boundary effect because the photospheric magnetic source concentrates near that axis. We calculated the potential energy with  $l = 20$ , 50, and 100, the result of which is shown in Figure 20. This figure shows that there is a difference among those three cases, though such a difference becomes smaller as we make a comparison between larger  $l$  cases. On the basis of this result, we safely estimate the potential energy from the  $l = 100$  case all through this study.

#### REFERENCES

- Amari, T., Luciani, J. F., Mikic, Z., & Linker, J. 2000, *ApJ*, 529, L49  
 Caligari, P., Moreno-Insertis, F., & Schüssler, M. 1995, *ApJ*, 441, 886  
 Canfield, R. C., Hudson, H. S., & McKenzie, D. E. 1999, *Geophys. Res. Lett.*, 26, 627  
 Choudhuri, A. R., & Gilman, P. A. 1987, *ApJ*, 316, 788  
 D'Silva, S., & Choudhuri, A. R. 1993, *A&A*, 272, 621  
 Emonet, T., & Moreno-Insertis, F. 1998, *ApJ*, 492, 804  
 Fisher, G. H., Fan, Y., & Howard, R. F. 1995, *ApJ*, 438, 463  
 Howard, R. F. 1991, *Sol. Phys.*, 136, 251  
 Ishii, T. T., Kurokawa, H., & Takeuchi, T. T. 1998, *ApJ*, 499, 898  
 Kaisig, M., Tajima, T., Shibata, K., Nozawa, S., & Matsumoto, R. 1990, *ApJ*, 358, 698  
 Kankelborg, C. C., & Longcope, D. W. 1999, *Sol. Phys.*, 190, 59–77  
 Krall, J., Chen, J., Santoro, R., Spicer, D. S., Zalesak, S. T., & Cargill, P. J. 1998, *ApJ*, 500, 992  
 Longcope, D. W., Fisher, G. H., & Arendt, S. 1996, *ApJ*, 464, 999  
 Low, B. C. 1994, *Plasma Phys.*, 1, 1684  
 Magara, T. 1998, Ph.D. thesis, Univ. Kyoto  
 Magara, T., & Shibata, K. 1999, *ApJ*, 514, 456  
 Matsumoto, R., Tajima, T., Chou, W., Okubo, A., & Shibata, K. 1998, *ApJ*, 493, L43  
 Moreno-Insertis, F., & Emonet, T. 1996, *ApJ*, 472, L53  
 Nozawa, S., et al. 1992, *ApJS*, 78, 267  
 Parker, E. N. 1966, *ApJ*, 145, 811  
 ———. 1979, *Cosmical Magnetic Fields* (Oxford: Oxford Univ. Press)  
 Priest, E. R. 1982, in *Solar Magnetohydrodynamics* (Dordrecht: Reidel), 256  
 Schmieder, B., Demoulin, P., Aulanier, G., & Golub, L. 1996, *ApJ*, 467, 881  
 Schüssler, M. 1979, *A&A*, 71, 79  
 Shibata, K., Tajima, T., & Matsumoto, R. 1990, *Phys. Fluids B*, 2  
 Shibata, K., Tajima, T., Steinolfson, R. S., & Matsumoto, R. 1989, *ApJ*, 345, 584  
 Solanki, S. 1994, *Space Sci. Rev.*, 63, 1  
 Spruit, H. C. 1979, *Sol. Phys.*, 61, 363  
 ———. 1981, *A&A*, 98, 155  
 Steiner, O., Grossmann-Doerth, U., Knoelker, M., & Schüssler, M. 1998, *ApJ*, 495, 468  
 Stix, M. 1991, in *The Sun: An Introduction* (Berlin: Springer), 194  
 Tajima, T., & Shibata, K. 1997, in *Plasma Astrophysics* (Massachusetts: Addison-Wesley), 189  
 Takeuchi, A. 1993, *PASJ*, 45, 811  
 Tanaka, K. 1991, *Sol. Phys.*, 136, 133  
 Thomas, J. H., & Weiss, N. O. 1992, in *Proc. NATO Advanced Research Workshop, Sunspots: Theory and Observations*, ed. J. H. Thomas & N. O. Weiss (Cambridge: Kluwer), 3–59  
 van Ballegoijen, A. A., & Martens, P. C. H. 1989, *ApJ*, 343, 971  
 Yokoyama, T., & Shibata, K. 1996, *PASJ*, 48, 353  
 Yoshimura, K., & Kurokawa, H. 1999, *ApJ*, 517, 964